



# Constrained nonlinear high-efficiency model predictive techniques for test mass capture

Yuxian Liu<sup>a</sup>, Yan Li<sup>a</sup>, Pengcheng Wang<sup>b</sup>, Yonghe Zhang<sup>b,\*</sup>

<sup>a</sup> School of Automation, Northwestern Polytechnical University, Shaanxi 710129, PR China

<sup>b</sup> Innovation Academy for Microsatellites, Chinese Academy of Sciences (CAS), Shanghai 201203, PR China

Received 30 September 2022; received in revised form 23 February 2023; accepted 28 February 2023

Available online 10 March 2023

---

## Abstract

This paper presents a nonlinear high-efficiency model predictive control (NHMPC) with constraints designed for the test mass (TM) capture phase of the drag-free satellite about gravitational wave observatory. To avoid collisions between test mass and satellite cavity, TM capture is the essential technology for drag-free satellite. Test mass is located inside an electrostatic suspension and locked by a clamp mechanism initially. The test masses are released with high initial offsets and velocities when the mechanism is retracted. The purpose of this phase is to guarantee the TM to be positioned at the cage center and attitude aligned with the local cage frame. Due to the low actuation authority of electrostatic suspension along with critical initial offsets and velocities, it is a challenging task to design the attitude and translation control schemes with simultaneous consideration of system performance and energy consumption. For the problem given above, the TM capture can be reformulated into a nonlinear quadratic optimal control problem with the state and input constraints. A nonlinear model predictive control (NMPC) structure is also designed to handle the noises by forming a closed loop. This control framework can realize optimality and robustness in a compromise. To improve the speed of solving high-dimensional nonlinear optimal control online for MPC, the indirect Chebyshev pseudospectral method with constraints is employed. The convergence and stability of the control loop are analyzed. Simulation examples show that the feasibility and performance of the designed control loop are verified compared with the existing methods and computation times in the millisecond range can be achieved.

© 2023 Published by Elsevier B.V. on behalf of COSPAR.

**Keywords:** Drag-free satellite; Test mass capture; Model predictive control; Indirect pseudospectral method

---

## 1. Introduction

Over the last years, the field of drag-free satellites has gained increasing interest in the detection of gravitational waves ([Armano et al. \(2016\)](#); [Lian et al. \(2021a\)](#); [Gong et al. \(2021\)](#); [Ruan et al. \(2020\)](#)). Drag-free satellites usually

adopt test mass (TM) without any mechanical contact to reduce the influence of mechanical structure. Each test mass is a cubic body located inside an electrostatic suspension and constrained firmly inside its hosting housing by a dedicated mechanism at launch, named caging and vent mechanism (CVM) ([Zanoni and Bortoluzzi \(2014\)](#), [Zanoni et al. \(2015\)](#), [Armano et al. \(2015\)](#)). During the in-orbit phase, to initialize the science operations, the TMs had to be set into free-fall and then controlled to the geodesic trajectory. The injection of the TMs into free-fall was performed by the grabbing positioning and

---

\* Corresponding author.

E-mail addresses: [liuyxian@mail.nwpu.edu.cn](mailto:liuyxian@mail.nwpu.edu.cn) (Y. Liu), [liyan@nwpu.edu.cn](mailto:liyan@nwpu.edu.cn) (Y. Li), [wangpc@microstate.com](mailto:wangpc@microstate.com) (P. Wang), [zhangyh@microstate.com](mailto:zhangyh@microstate.com) (Y. Zhang).

release mechanism (GPRM) (Bortoluzzi et al. (2021)). Thus, the capture of TM is essential for the whole space mission. The state error, also known as "control accuracy", caused by the GPRM in this process has attracted widely the attention of researchers.

Unfortunately, the clamp mechanism was already tested in flight by the technological demonstrator LISA Pathfinder in 2016, obtaining a release performance worse than expected due to the improper high initial velocities (Bortoluzzi et al. (2016)). Due to the high initial velocities, the test masses hit the plungers. To address the problem, most of the previous work has focused only on preventing collision between TM and cavity. In (Lian et al. (2021b)), a general solution is given for test mass release points to minimize the relative motion between the test mass and the satellite mass center. A sliding mode control based on RBF neural network is designed to accommodate attitude-orbit modeling with 12 degrees of freedom for the test mass release in (Lian et al. (2022)). After losing part of their kinetic energy, the sliding mode controllers were able to capture the test masses by means of the electrostatic suspensions (Schleicher et al. (2018)). Later in (Vidano et al. (2022)), the paper utilizes a model predictive control (MPC) design for the test mass release phase of the LISA space mission, which is part of the LISA DFACS preliminary prototyping study of the European Space Agency.

The robust stabilization control schemes for drag-free satellites work by linearizing the nonlinear models and different decoupling SISO control loops. Those methods evidently suffer from degraded performance subject to the deviation between true initial states and desired states. In practical flight drag-free applications, other crucial factors that guarantee the successful capture of test masses are weak electrostatic forces, noise, and state constraints. Compared with the robustness in the scientific measurement mode, it is expected to use as little energy as possible to return TM to the center of the electrode cage and stabilize after the TM release. And this process can be generalized into a nonlinear quadratic optimal problem that simultaneously consideration of error performance and energy consumption. So far, hardly any control law incorporating these aspects has been reported to the best of the author's knowledge. Considering the suppression of external disturbance and parameter uncertainty, model predictive control (MPC) is a more suitable method. MPC is often applied to many aerospace engineering problems (Allenspach and Ducard (2021); Li et al. (2020); Chai et al. (2018); Zidek et al. (2018); Deng and Ohtsuka (2019); Deng and Ohtsuka (2022); Deng and Ohtsuka (2018)).

The solving of nonlinear optimal control in the MPC is complicated and troublesome, which causes worse real-time performance. In the linear MPC case, Wang et al. (Wang and Boyd (2009)) exploit the specific problem structure of MPC to decrease the time complexity of solving the

resulting quadratic program (QP). Though numerical results demonstrate the effectiveness of QP in handling the constrained nonlinear optimal control problems (OCPs), the QP techniques might still result in a decrease in calculation efficiency when compared with the indirect pseudospectral approaches in the nonlinear case (Wang and Li (2021)). This is because the indirect pseudospectral method (IPM) transforms nonlinear quadratic optimal control problems (QOCP) into a series of linear equations instead of handling Riccati equation. Thus, the indirect pseudospectral method has high computational efficiency in dealing with constrained optimal problems. The background of IPM under NMPC framework is based on Pontryagin's principle (Pontryagin et al. (1962)). In other words, Two-Points Boundary Value Problem (TPBVP) equation is obtained through Pontryagin's principle (Pagone et al. (2022)). Moreover, Pontryagin-based nonlinear model predictive control (NMPC) is also the main solving method for NMPC, which has a certain fundamental theoretical (Lemos (2010), Cannon et al. (2008)). In order to better apply MPC to TM release and capture, the indirect pseudospectral method is a significant part of TM release and capture problem. We hope that IPM can take advantage of this feature and make MPC better real-time computing capability. Inspired by previous work, a nonlinear high-efficiency model predictive control with constraints for the test mass capture phase is proposed to meet the engineering application requirements as much as possible in this paper.

The main contribution of this work is the development of a nonlinear MPC module for the test mass capture phase, capable of covering the optimal characteristic with constraint conditions, handling the nonlinear dynamics and improving the real-time computational efficiency without the need for QP transcription and Riccati equation calculation. Compared with the simulation proof-of-concept provided in the existing references, the controller in this work has improved the performance in terms of transient, real-time and steady-state error.

- For the first time, the TM capture phase is reformulated to a nonlinear QOCP with constraints. A nonlinear model predictive control method is used, which comprehensively considers robustness and optimality at one time and does not need to consider the problem of model decoupling.
- The task of solving nonlinear QOCP is difficult and complicated evidently due to the high-dimensional relative dynamics of TM. A high-efficiency model predictive control algorithm based on the indirect Chebyshev pseudospectral method (ICPM) is proposed for TM capture. The proposed MPC framework allows one to easily incorporate state and control constraints including mixed state and control constraints, which integrates constraints into the nonlinear quadratic optimal control problem and is solved by numerical

method. The designed controller can address the nonlinear characteristic of the system and minimize the objective consisting of energy consumption and state errors under the premise of the relative angle and position constraints of the TM. The proposed method improves computational efficiency and guarantees feasibility in real-time, which is more in line with engineering practice.

The theoretical background and key ideas of this novel approach are explained in the remainder of the paper. The nonlinear dynamics of the test mass used for controller synthesis is derived in Section 2. Key ideas behind the nonlinear MPC, as well as the underlying optimization problem formulation and incorporated solver are presented in Section 3. A theoretical derivation of the indirect pseudospectral method also performed in this section accounts for state and input constraints and efficiently exploits the spectral discretization to solve the optimal controller expediently and rapidly. The numerical simulations conducted to evaluate the feasibility and performance of the proposed approach are discussed in Section 4. Additionally, simulation results for comparison against existing methods are included. Finally, Section 5 concludes with remarks and possible directions for future work.

## 2. Plant description

In this paper, the optimal robust problem for the test mass under the inertia matrix uncertainties and external noises is considered. Firstly, the relative motion of the TM with respect to the cavity is established (Lian et al. (2022)). Let  $O_{xyz}, O_i x_i y_i z_i, O'_i x'_i y'_i z'_i, (i = 1, 2)$  denote the Satellite Centered Orbit frame, Satellite cavity frame and TM body frame, respectively.

### 2.1. Relative translation dynamics

The drag-free satellite system consists of two cubic TMs with measurement and actuation provisions along all degrees of freedom. For drag-free satellites, one core technology for achieving the mission requirements is the attitude-orbit control of the test mass after release (see Fig. 1). This paper assumes that the satellite has achieved good stability. Considering that TM1 and TM2 are independent of each other, it can easily get the relative translational dynamics between TM and the mass center of the satellite as follows.

The relative motion of the TM with respect to the cavity is important. Therefore, the relative translation dynamics in  $O_i x_i y_i z_i$  can be written as follows.

$$\begin{aligned} m\ddot{\mathbf{r}}_{ri} - m\mathbf{A}_r(r'_{oi}, \omega_0, \dot{\omega}_0)\mathbf{r}_{ri} + m\mathbf{B}_r(r'_{oi}, r_0) \\ - m\mathbf{D}_r(r'_{oi}, \omega_0, \dot{\omega}_0)\mathbf{r}_{il} = \mathbf{S}\mathbf{F}_i + \mathbf{S}\mathbf{f}_i \end{aligned} \quad (1)$$

where

$$\begin{aligned} \mathbf{F}_{io} &= [F_{iox}, F_{ioy}, F_{ioz}]^T \\ \mathbf{f}_{io} &= [f_{iox}, f_{ioy}, f_{ioz}]^T \\ \mathbf{r}_{ri} &= [r_{ix}, \dot{r}_{ix}, r_{iy}, \dot{r}_{iy}, r_{iz}, \dot{r}_{iz}]^T, \\ \mathbf{r}_{il} &= [r_{ilx}, r_{ily}, r_{ilz}]^T, \\ \mathbf{B}_r(r'_{oi}, r_0) &= \frac{\mu}{r'^3_{oi}} r_o [0, \sin \alpha, 0, 0, 0, -\cos \alpha]^T \\ \mathbf{S} &= \begin{bmatrix} 0 & 1 & 0 & 0 & 0 & 0 \\ 0 & 0 & 0 & 1 & 0 & 0 \\ 0 & 0 & 0 & 0 & 0 & 1 \end{bmatrix}^T \\ \mathbf{A}_r(r'_{oi}, \omega_0, \dot{\omega}_0) &= \begin{bmatrix} 0 & 1 & 0 & 0 & 0 & 0 \\ -\frac{\mu}{r'^3_{oi}} + \omega_0^2 & 0 & 0 & 0 & -\dot{\omega}_0 & -2\omega_0 \\ 0 & 0 & 0 & 1 & 0 & 0 \\ 0 & 0 & -\frac{\mu}{r'^3_{oi}} & 0 & 0 & 0 \\ 0 & 0 & 0 & 0 & 0 & 1 \\ \dot{\omega}_0 & 2\omega_0 & 0 & 0 & -\frac{\mu}{r'^3_{oi}} + \omega_0^2 & 0 \end{bmatrix} \end{aligned} \quad (2)$$

$$\begin{aligned} \mathbf{D}_r(r'_{oi}, \omega_0, \dot{\omega}_0) &= \begin{bmatrix} -\cos \alpha & 0 & \sin \alpha \\ \left(-\frac{\mu}{r'^3_{oi}} + \omega_0^2\right) \cos \alpha - \dot{\omega}_0 \sin \alpha & 0 & -\left(-\frac{\mu}{r'^3_{oi}} + \omega_0^2\right) \sin \alpha - \dot{\omega}_0 \cos \alpha \\ 0 & -1 & 0 \\ 0 & -\frac{\mu}{r'^3_{oi}} & 0 \\ -\sin \alpha & 0 & -\cos \alpha \\ \dot{\omega}_0 \cos \alpha + \left(-\frac{\mu}{r'^3_{oi}} + \omega_0^2\right) \sin \alpha & 0 & -\dot{\omega}_0 \sin \alpha + \left(-\frac{\mu}{r'^3_{oi}} + \omega_0^2\right) \cos \alpha \end{bmatrix} \end{aligned}$$

where  $m$  is the mass of TM,  $\mu$  is a standard gravitational parameter.  $r_o$  denotes the distance from Earth's mass center to satellite's mass center.  $r'_{oi} = \sqrt{x_i^2 + y_i^2 + (r_o + z_i)^2}$  is the distance between TM's mass center and Earth's mass center.  $\omega_0$  and  $\dot{\omega}_0$  express the orbital angular velocity and angular acceleration, respectively.  $(r_{iz}, r_{iy}, r_{iz})^T$  and  $(\dot{r}_{iz}, \dot{r}_{iy}, \dot{r}_{iz})^T$  denote the position vector and the velocity vector of TM in  $O_i x_i y_i z_i$ , respectively.  $(r_{ilx}, r_{ily}, r_{ilz})^T$  is the position of the cavity center relative to the satellite mass center.  $\alpha = 60^\circ$  or  $120^\circ$  is a rotational angle from  $O_{xyz}$  to  $O_i x_i y_i z_i$  around the y-axis.  $\mathbf{F}_i$  and  $\mathbf{f}_i$  are the control force and the disturbance force in  $O_i x_i y_i z_i$ , respectively.

### 2.2. Relative attitude dynamics

Assuming  $r_{il}$  does not change with time. By theoretical derivation, a general Euler equation can be written as

$$\mathbf{J}_i \dot{\boldsymbol{\omega}}_i + \boldsymbol{\omega}_i \times \mathbf{J}_i \boldsymbol{\omega}_i = \mathbf{M}_i \quad (3)$$

where  $\mathbf{J}_i$  is the rotational inertia of TM,  $\mathbf{M}_i$  denotes the control torque vector,  $\boldsymbol{\omega}_i$  expresses the angular velocity of rotation,  $\dot{\boldsymbol{\omega}}_i$  is the angular acceleration of rotation.

The attitude angular velocity of the TM can be written as

$$\begin{bmatrix} \omega_{ix} \\ \omega_{iy} \\ \omega_{iz} \end{bmatrix} = \begin{bmatrix} 1 & 0 & -\sin \theta \\ 0 & \cos \varphi_i & \sin \varphi_i \cos \theta \\ 0 & -\sin \varphi_i & \cos \varphi_i \cos \theta \end{bmatrix} \begin{bmatrix} \dot{\phi}_i \\ \dot{\theta}_i \\ \dot{\psi}_i \end{bmatrix} + \mathbf{C}_{ib} \begin{bmatrix} 0 \\ \omega_0 \\ 0 \end{bmatrix} \quad (4)$$

where

$$\mathbf{C}_{ib} = \begin{bmatrix} \cos \alpha & 0 & -\sin \alpha \\ 0 & 1 & 0 \\ \sin \alpha & 0 & \cos \alpha \end{bmatrix} \mathbf{C}_{x0}.$$

$\mathbf{C}_{x0}$  is direction cosine matrix.  $\omega_0 = \sqrt{\frac{\mu}{p^3}}(1 + e \cos \theta)^2$ ,  $p$  is the semi-parameter.  $e$  denotes the eccentricity,  $\theta$  expresses the true anomaly.  $(\varphi_i, \theta_i, \psi_i)^T$  and  $(\dot{\varphi}_i, \dot{\theta}_i, \dot{\psi}_i)^T$  denote the attitude angle and the attitude angular velocity of the  $i$ th TM, respectively.

Considering the minor attitude angle (The range can see the Appendix), the sine and cosine functions can be approximated as  $\sin \varphi_i \approx \varphi_i, \cos \varphi_i \approx 1$ .

For Eq. (4), higher-order terms are ignored.

$$\begin{bmatrix} \omega_{ix} \\ \omega_{iy} \\ \omega_{iz} \end{bmatrix} = \begin{bmatrix} \dot{\varphi}_i \\ \dot{\theta}_i \\ \dot{\psi}_i \end{bmatrix} + \begin{bmatrix} \psi_i \cos \alpha + \varphi_i \sin \alpha - \theta_i \psi_i \sin \alpha \\ 1 \\ \psi_i \sin \alpha - \varphi_i \cos \alpha + \theta_i \psi_i \cos \alpha \end{bmatrix} \omega_0 \quad (5)$$

Differentiating Eq. (5), we get

$$\begin{bmatrix} \dot{\omega}_{ix} \\ \dot{\omega}_{iy} \\ \dot{\omega}_{iz} \end{bmatrix} = \begin{bmatrix} \ddot{\varphi}_i \\ \ddot{\theta}_i \\ \ddot{\psi}_i \end{bmatrix} + \begin{bmatrix} \dot{\psi}_i \cos \alpha + \dot{\varphi}_i \sin \alpha \\ 0 \\ \dot{\psi}_i \sin \alpha - \dot{\varphi}_i \cos \alpha \end{bmatrix} \omega_0 + \begin{bmatrix} \psi_i \cos \alpha + \varphi_i \sin \alpha - \theta_i \psi_i \sin \alpha \\ 1 \\ \psi_i \sin \alpha - \varphi_i \cos \alpha + \theta_i \psi_i \cos \alpha \end{bmatrix} \dot{\omega}_0 \quad (6)$$

Substituting Eq. (5) and Eq. (6) into Eq. (3), and the cubic TM and disturbance are considered as

$$\begin{aligned} J_i \dot{\zeta}_i - \mathbf{J}_i \mathbf{A}_\zeta(\omega_0, \dot{\omega}_0, \alpha) \zeta_i - \\ = \mathbf{SM}_i + \mathbf{ST}_i \end{aligned} \quad (7)$$

where  $\mathbf{J}_i = \text{diag}(J_{ix}, J_{iy}, J_{iz})$ ,

$\zeta_i = [\varphi_i, \dot{\varphi}_i, \theta_i, \dot{\theta}_i, \psi_i, \dot{\psi}_i]^T$ .  $\mathbf{T}_i$  is disturbance torque.

$\mathbf{A}_\zeta(\omega_0, \dot{\omega}_0, \alpha) =$

$$\begin{bmatrix} 0 & 1 & 0 & 0 & 0 & 0 \\ -\dot{\omega}_0 \sin \alpha & -\omega_0 \sin \alpha & 0 & 0 & -\dot{\omega}_0 \cos \alpha & -\omega_0 \cos \alpha \\ 0 & 0 & 0 & 1 & 0 & 0 \\ 0 & 0 & 0 & 0 & 0 & 0 \\ 0 & 0 & 0 & 0 & 0 & 1 \\ \dot{\omega}_0 \cos \alpha & \omega_0 \cos \alpha & 0 & 0 & -\dot{\omega}_0 \sin \alpha & -\omega_0 \sin \alpha \end{bmatrix}$$

$$\mathbf{B}_\zeta(\theta_i, \psi_i, \dot{\omega}_0, \alpha) = [0, \theta_i \psi_i \dot{\omega}_0 \sin \alpha, 0, -\dot{\omega}_0, 0, -\theta_i \psi_i \cos \alpha]^T, \quad \mathbf{M}_i = [M_{ix}, M_{iy}, M_{iz}]^T, \quad \mathbf{T}_i = [T_{ix}, T_{iy}, T_{iz}]^T$$

According to Eq. (1) and Eq. (7), we get

$$\begin{aligned} \begin{bmatrix} \dot{\mathbf{r}}_{ri} \\ \dot{\zeta}_i \end{bmatrix} = & \begin{bmatrix} \mathbf{A}_r(r'_{oi}, \omega_0, \dot{\omega}_0) & 0 \\ 0 & \mathbf{A}_\zeta(\omega_0, \dot{\omega}_0, \alpha) \end{bmatrix} \begin{bmatrix} \mathbf{r}_{ri} \\ \zeta_i \end{bmatrix} \\ & + \begin{bmatrix} -\mathbf{B}_r(r'_{oi}, r_0) \\ \mathbf{B}_\zeta(\theta_i, \psi_i, \dot{\omega}_0, \alpha) \end{bmatrix} + \begin{bmatrix} \mathbf{D}_r(r'_{oi}, \omega_0, \dot{\omega}_0) r_{il} \\ 0 \end{bmatrix} \\ & + \begin{bmatrix} \frac{1}{m_{x,y,z}} & 0 \\ 0 & \frac{1}{j_i} \end{bmatrix} \begin{bmatrix} \mathbf{SF}_i + \mathbf{Sf}_i \\ \mathbf{SM}_i + \mathbf{ST}_i \end{bmatrix} \end{aligned} \quad (8)$$

Eq. (8) is the attitude-orbit dynamics model with 12 degrees of freedom after the drag-free satellite's two test masses release.

**Remark 1.** The disturbances  $\mathbf{f}_i$  and  $\mathbf{T}_i$  include solar pressure noises, local environmental noises, measure noises, constant noises and actuation noises. Moreover, if the angle between the two telescopes is changed, Eq. (8) can be extended to 13 degrees of freedom by considering the change of  $\alpha$ .

### 3. Control design

In this section, three parts of the NHMPC are introduced for the TM capture, including model predictive method with closed-loop, open-loop optimal control and spectral discretization. Model predictive control (MPC) or receding horizon control (RHC) is a form of control in which the current control action is obtained by solving online, at each sampling instant, a finite horizon open-loop optimal control problem, using the current state of the plant as the initial state. The optimization yields an optimal control sequence and the first control in this sequence is applied to the plant (Mayne et al. (2000)). When solving the optimal value in the prediction horizon regardless of the parameter uncertainties and external disturbances, such a case is equivalent to offline solution or open-loop control. This expression is also used in (Mayne et al. (2000), Palanki et al. (1993)). The output is calculated in the whole prediction horizon without the influence of real-time feedback disturbances and other factors. The MPC of closed-loop control is due to continuous receding using the optimal controller in the prediction horizon. The operation of each sampling period will use the actual model with uncertainties and time variant disturbances. This flow is similar to closed-loop control. Thus, this paper describes this receding horizon process as closed-loop control.

For the control of the position and attitude after the TM is released, the control framework is designed in this section. As already mentioned in Section 1, the controller must be able to handle the noises and uncertainties associated with the solar radiation pressure, the electrostatic coupling force, etc. Additionally, the interior optimal controller is also expected to minimize the objective consisting of energy consumption and state errors. We proposed the control architecture shown in Fig. 2 and Fig. 3 to tackle these challenges. To simplify, the single TM is

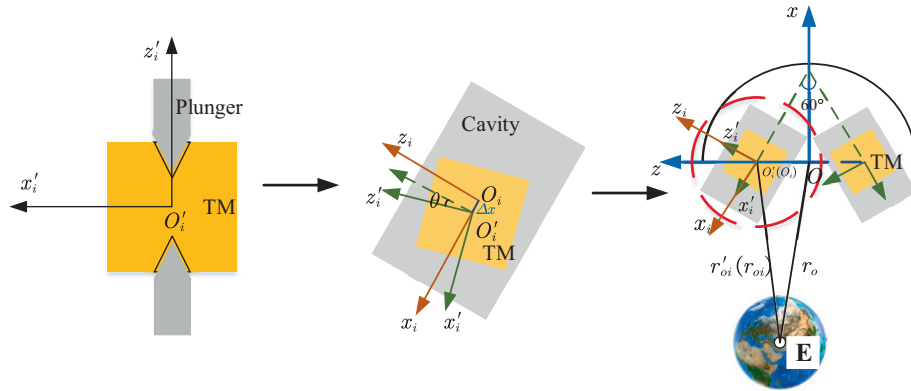


Fig. 1. The reference coordinate system for TM capture.

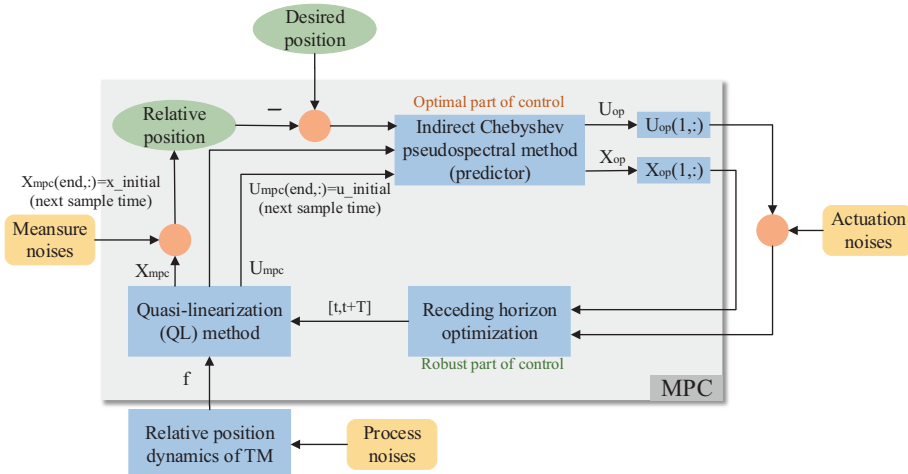


Fig. 2. The control frame of relative position control.

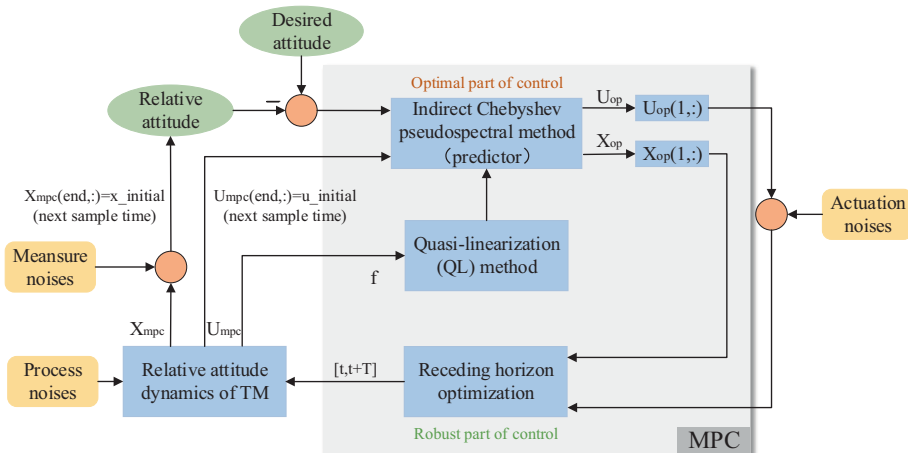


Fig. 3. The control frame of relative attitude control.

considered in this paper. This section focuses on the MPC framework which ensures feasible control and state trajectories generation under nonlinear dynamics, including dynamics processing and problem formulation.

TM dynamics is designed in two parts: relative displacement and relative angle of TM. Each part is a 6-DOF model. The reduction of model order can improve the accuracy and speed of numerical calculation. The quasilinearization method, which has the benefit of making controllers convenient to calculate, is used to create the model with nonlinear properties. The prediction horizon length is chosen. The process of TM capture in the prediction horizon is regarded as an optimal quadratic problem in the finite domain, and ICPM is employed to solve the open-loop optimal controller of this problem. The initial value of the open-loop controller is applied to a single sampling period to obtain the optimal state trajectory under the influence of noises in the sampling period. This method allows for the real-time solution to form the closed-loop controller.

### 3.1. Model predictive method with closed-loop control

Without loss of generality, assume that  $\mathbf{d}$  is the random noise.  $\mathbf{d} \in \mathcal{D}$ ,  $\mathcal{D}$  is a nonempty, compact and convex set,  $\mathcal{D} \subset \mathbb{R}^{12}$ .  $D \triangleq \sup_{\mathbf{d}(t) \in \mathcal{D}} \|\mathbf{d}(t)\|$ .  $\mathbf{d}$  can represent process noises, actuation noises and measure noises, which are unavoidable external disturbances affecting the control accuracy for TM capture. Eq. (8) can be written in nonlinear affine form as shown in Eq. (9).

$$\dot{\mathbf{x}}(t) = \mathbf{f}(\mathbf{x}) + \mathbf{g}(\mathbf{x})\mathbf{u} + \mathbf{d} \quad (9)$$

where  $\mathbf{u} = [\mathbf{F}_i; \mathbf{M}_i]^T \in \mathbb{R}^6$  is the control input variable vector,  $\mathbf{x} = [\mathbf{r}_i; \boldsymbol{\zeta}_i]^T \in \mathbb{R}^{12}$  is the state variable vector.  $\mathbf{d} = [\mathbf{f}_i; \mathbf{T}_i]^T \in \mathbb{R}^6$ .

Otherwise, the state and control constraints need to be incorporated into the calculation process due to the mechanical structure for TM capture. The top-level goal is to avoid the test mass from touching the housing hinting at the constraints of relative position and angle. This also implies that the smaller TM's displacement is, the better. Since the electrodes can only pull, and their pull becomes weaker as the TM displacement grows, it becomes more likely that the electrostatic force will not be sufficient to prevent it. Thus, the input constraints are also considered to avoid the desired control force and torque beyond the maximum. The whole process of designing the controller can be regarded as the **Problem 1**.

**Problem 1.** Consider the continuous-time quadratic optimal control problem formulation (10) in prediction horizon  $T_1$ . The sample time is set to  $T$ .

To minimize

$$J^{(k)} = \int_{t_k}^{t_0^{(k)}+T} \frac{1}{2} \left[ (\mathbf{x}^{(k)}(t) - \mathbf{x}_d)^T \mathbf{Q}(x) (\mathbf{x}^{(k)}(t) - \mathbf{x}_d) + \mathbf{u}^{(k)T}(t) \mathbf{R} \mathbf{u}^{(k)}(t) \right] dt \quad (10)$$

subject to

$$\begin{aligned} \dot{\mathbf{x}}(t) &= f(\mathbf{x}^{(k)}(t), \mathbf{u}^{(k)}(t)) \\ \mathbf{x}^{(k)}(t_0) &= \mathbf{x}_0^{(k)} \\ \alpha_{\min}^i \leq x_i^{(k)} \leq \alpha_{\max}^i, i &= 1, \dots, n \\ \beta_{\min}^i \leq u_i^{(k)} \leq \beta_{\max}^i, i &= 1, \dots, m \end{aligned} \quad (11)$$

where  $x_i$  and  $u_i$  are the elements of  $\mathbf{x}$  and  $\mathbf{u}$ , respectively.  $\alpha_{\min}^i, \alpha_{\max}^i, \beta_{\min}^i, \beta_{\max}^i$  are the lower and upper bounds.

The total cost is

$$J_M(\mathbf{x}, \mathbf{u}) = \sum_{k=0}^{M-1} J^{(k)} + J_f(\mathbf{x}^M) \quad (12)$$

$J_f(\cdot)$  is the terminal penalty on the final state. The number of sampling periods is  $M - 1$ .  $\mathbf{x}_d$  is the desired state.

**Problem 1** is defined to describe the MPC algorithm. A terminal cost is removed in the cost function to estimate the cost of completing the reconfiguration from the state and time at the process of the optimization horizon ([Morgan et al. \(2014\)](#)). The application of the proposed MPC scheme for the TM capture problem is demonstrated through a flowchart given in [Fig. 2](#) and [Fig. 3](#). The process of the control algorithm is now described in [Algorithm 1](#).

**Remark 2.** The length of prediction horizon  $T_1$  will influence the solving accuracy of the TM capture controller. If the prediction horizon is too short, it easily leads to an unstable tracking effect. The model prediction is insufficient and the effect may not be good. The dynamic process performance of the whole MPC deteriorates, which in turn leads to the violation of accuracy requirements. If the prediction horizon is long, the calculation cost can be huge, and data processing is complex. Therefore, an appropriate value should be taken in the middle. The prediction horizon needs to be selected reasonably according to the requirements, simulation conditions and parameter experience. The capability of addressing external disturbances depends on the value of sampling time  $T$ . This is because the robustness of MPC relies on the closed-loop with the real-time feedback of states and inputs.

The stopping criterion of nonlinear MPC can be defined as

$$\frac{\|\mathbf{x}^{(k)} - \mathbf{x}_d\|}{\|\mathbf{x}^{(k-1)} - \mathbf{x}_d\|} \leq \varepsilon_1 \quad (13)$$

**Algorithm 1.** High-efficiency model predictive algorithm

- 
- 1: *Initialization:* Start with initial state  $x_0$ , sample time  $T$ , the prediction horizon  $T_1$  in time domain  $[t_0, +\infty], k = 0$ . The  $k$  represents the  $k$ th sampling.
- 2: **procedure**
- 3: *Determine iterative optimal control:* Use the indirect Chebyshev pseudospectral method to calculate the optimal control problem subject to the nominal system in  $[t_0^{(k)}, t_0^{(k)} + T_1]$
- 4: *Determine real states in kth sample time:* Apply the first element of control sequence  $u(t)$  to the system for the single sample time  $T$ . The real states at the terminal point  $t_0^{(k)} + T$  are received.
- 5: Stop if the 2-norm of deviation between true relative states and desired states  $\|x - x_d\|$  is within a prescribed tolerance  $\varepsilon_1$  or the given iteration number is exceeded. Otherwise, use the terminal state points from the  $k$ th iteration as the next initial states, set  $k = k + 1$  and go to step 2.
- 6: **end procedure**
- 

### 3.2. Open-loop optimal control

The optimal problem of test capture for the drag-free satellite under the state and input constraints is described. The relative dynamics of TM is written in the nominal system, as shown in Eq. (14).

$$\begin{aligned} \dot{x}(t) &= f(x) + g(x)u \\ x(t_0) &= x_0, x(t_f) = x_f = x_e = 0 \end{aligned} \quad (14)$$

$$\tilde{g}(x, u, t) \leq 0 \quad (15)$$

where  $f(x(t), u(t))$  and  $g(x(t), u(t))$  are continuously differentiable nonlinear functions.  $x_0$  and  $x_f$  denote the initial state and terminal state on two endpoints  $t = 0$  and  $t = t_f$ , respectively. The specific form of  $\tilde{g}(x, u, t)$  is defined in (11). In this paper, the terminal state is equilibrium  $x_e$ . The length of  $[t_0, t_f]$  is the same as  $T_1$ .

**Problem 2.** Subjecting to the dynamic differential Eq. (14), the main objective of finite-horizon optimal control is to determine the state variables  $x \in \mathbb{R}^n$  and the control input  $u \in \mathbb{R}^m$  within the time interval  $t \in [t_0, t_f]$  to minimize the following Lagrange cost function.  $[t_0, t_f]$  is also the prediction horizon  $T_1$  in MPC.

$$J(x, u) = \frac{1}{2} \int_{t_0}^{t_f} \left( \|x - x_d\|_Q^2 + \|u\|_R^2 \right) dt \quad (16)$$

where  $Q$  and  $R$  are symmetric and positive-definite. Moreover, higher priority of  $Q$  is given to minimize the convergence time and output error. The larger values of  $R$  can make energy consumption reduction.

To solve the nonlinear optimal control problem, the second method of quasi-linearization is applied, in which the system Eq. (14) is expanded to the first-order form. The linear time-varying equation and the initial conditions are shown in Eq. (17)- Eq. (18).

$${}^{(p+1)}\dot{x}(t) = {}^{(p)}A(t) \quad (17)$$

$$x(t_0) = x_0, x(t_f) = x_e = 0$$

$${}^{(p)}h(t) = f({}^{(p)}x, {}^{(p)}u) - {}^{(p)}A(t){}^{(p)}x(t) - {}^{(p)}B(t){}^{(p)}u(t) \quad (18)$$

Without loss of generality, the state and input constraints in (19) and (20) are rewritten into

$${}^{(p)}C^{(p+1)}x + {}^{(p)}D^{(p+1)}u + {}^{(k)}v \leq 0 \quad (19)$$

$${}^{(p)}v(t) = g({}^{(p)}x, {}^{(p)}u, t) - {}^{(p)}C(t){}^{(p)}x(t) - {}^{(p)}D(t){}^{(p)}u(t) \quad (20)$$

where superscript  $p$  represents the  $p$ -th quasi-linearization iteration.  $A(t)$ ,  $B(t)$ ,  $C(t)$  and  $D(t)$  is the Jacobian matrix of dynamic equation.

In the following iterative solving process, the results obtained in the  $p$ th iteration are taken as the reference solutions for the  $(p+1)$ th iteration. And the iteration process goes on until the following convergent criterion achieves

$$\frac{\|{}^{(p+1)}c - {}^{(p)}c\|}{\|{}^{(p)}c - {}^{(p-1)}c\|} \leq \varepsilon_2 \quad (21)$$

where  ${}^{(p)}c$  is the solution (the relative states or inputs of TM) obtained in  $p$ th iterations. The variable  $\varepsilon_2$  is a small quantity that represents the convergent tolerance. To simplify the following derivations, we consider the problem without the iteration index.

By introducing a parametric variable  $\alpha$ , the inequality constraints in Eq. (19), are replaced by equality ones as

$$Cx + Du + v + \alpha = 0 \quad (22)$$

By introducing the costate vectors  $\lambda(t) \in \mathbb{R}^n$  and the Lagrangian multiplier  $\mu$ , Hamiltonian for this system can be expressed as

$$\begin{aligned} H = \frac{1}{2} & [x^T Qx + u^T Rx] + \lambda^T [Ax + Bu + h] \\ & + \mu^T [Cx + Du + v + \alpha] \end{aligned} \quad (23)$$

Based on the optimality condition for the constrained OCPs and according to the calculus of variations, we have costate equation

$$\dot{\lambda}(t) = -\frac{\partial H}{\partial x} = -[Q(t)x(t) + A^T(t)\lambda(t) + C^T(t)\mu(t)] \quad (24)$$

And based on the first order necessary conditions of optimal solution, the optimal control can be obtained

$$\frac{\partial H}{\partial u} = Ru + B^T\lambda + D^T\mu = 0 \quad (25)$$

$$u = -R^{-1}(B^T\lambda + D^T\mu) \quad (26)$$

By introducing a slack variable

$$\alpha = -Cx - Du - v \quad (27)$$

one has

$$\mu \geq 0 \quad (28)$$

$$\alpha \geq 0 \quad (29)$$

The complementarity slackness condition is given by

$$\mu^T \alpha = 0 \quad (30)$$

Based on the discussions above, the necessary conditions for the constrained system are given by

$$\begin{aligned} \dot{x}(t) &= A(t)x(t) - B(t)R^{-1}(t) \\ &\quad (B^T(t)\lambda(t) + D^T(t)\mu(t)) + h(t) \end{aligned} \quad (31)$$

$$\dot{\lambda}(t) = -[A^T(t)\lambda(t) + C^T(t)\mu(t) + Q^T(t)x(t)] \quad (32)$$

$$\begin{aligned} \alpha(t) &= -C(t)x(t) - v(t) + D(t)R^{-1}(t) \\ &\quad (B^T(t)\lambda(t) + D^T(t)\mu(t)) \end{aligned} \quad (33)$$

$$\mu(t) \geq 0 \quad (34)$$

$$\alpha(t) \geq 0 \quad (35)$$

$$\mu(t)^T \alpha(t) = 0 \quad (36)$$

The boundary conditions and transversality conditions are

$$\begin{cases} x(t=0) = x(t_0) = x_0 \\ \lambda(t_f) = P(t_f)x(t_f) = P(t_f)x_e \end{cases} \quad (37)$$

### 3.3. Spectral discretization

In order to use the solutions from the optimization problem as control inputs, a real-time nonlinear MPC solver with solving times in the millisecond range is required (The millisecond level is defined as within 100 ms ([Vidano et al. \(2022\)](#))). However, the high dimension dynamics for TM capture suffers from the well-known fundamental solving problems, such as ill-conditioned and decreasing computation speed, which is limited to engineering. The indirect pseudospectral methods differ from traditional indirect methods. This method can convert the resultant optimal control problem into a sequence of linear equations. Hence, optimal control can be solved rapidly and efficiently using basic matrix operations.

The optimal problem will be described in the interval  $[t_0, t_f]$ . The state and costate trajectories of TM are approximated by a Lagrange polynomial using Chebyshev-Gauss-Lobatto (CGL) points. Since CGL points lie in the interval  $[-1, 1]$ , the prediction horizon  $[t_0, t_f]$  for optimal problem is transformed to the interval  $[-1, 1]$  by the following time transformation.

$$\tau = \frac{2t - (t_0 + t_f)}{t_f - t_0} \quad (38)$$

and the corresponding derivative

$$T(\tau) = \dot{\Psi}(\tau) = \frac{t_f - t_0}{2} \quad (39)$$

where  $t \in [t_0, t_f]$ ,  $\tau \in [-1, 1]$ . The initial position and angle of TM are represented by  $x(\tau = -1) = x_0$ . The corresponding terminal costate are satisfied with  $\lambda(\tau = 1) = Px_f$ .

The discretization process begins by approximating the continuous state and control variables by  $N$ th polynomials of the form

$$x \approx X = \sum_{l=0}^N X_l \phi_l(\tau) \quad (40)$$

$$\lambda \approx \Lambda = \sum_{l=0}^N \Lambda_l \phi_l(\tau) \quad (41)$$

And the CGL points  $(\tau_0, \dots, \tau_l, \dots, \tau_N)$  are defined as

$$t_l = \cos\left(\frac{N-l}{N}\pi\right), l = 0, 1, \dots, N \quad (42)$$

where  $\tau_0 = -1$ ,  $\tau_N = 1$ . These points are the extrema of the  $N$ th order Chebyshev polynomial  $T_N(t) = \cos(N \arccos t)$ . For  $l = 0, 1, \dots, N$ ,  $\phi_l(\tau)$  are the Lagrange interpolating polynomials of  $N$ .

$$\phi_l(\tau) = \frac{(-1)^{l+1}(1-\tau^2)\dot{T}_N(\tau)}{N^2 c_l(t-t_l)}, c_l = \begin{cases} 2, l = 0, N \\ 1, 1 \leq l \leq N-1 \end{cases} \quad (43)$$

Then, the derivative of  $x$  and  $\lambda$  at the quadrature node  $\tau$  is easily computed by the matrix  $V$  in Eq. (45).

$$\dot{x}(\tau_r) \approx \dot{X}(\tau_r) = \sum_{l=0}^N X(\tau_l) \dot{\phi}_l(\tau_r) = \sum_{l=0}^N V_{rl} X(\tau_l) \quad (44)$$

$$\dot{\lambda}(\tau_r) \approx \dot{\Lambda}(\tau_r) = \sum_{l=0}^N \Lambda(\tau_l) \dot{\phi}_l(\tau_r) = \sum_{l=0}^N V_{rl} \Lambda(\tau_l)$$

$V_{rl}$  are the entries of the  $(N+1) \times (N+1)$  differentiation matrix  $V$ :

$$V_{rl} = \begin{cases} (c_l/c_r)[(-1)^{r+l}/(\tau_r - \tau_l)] & r \neq l \\ \tau_l/(2 - 2\tau_l^2) & 1 \leq r = l \leq N-1 \\ -(2N^2 + 1)/6 & r = l = 0 \\ (2N^2 + 1)/6 & r = l = N \end{cases} \quad (45)$$

Then, the discrete TPBVP defined by [Eq. \(46\)–\(47\)](#) is algebraic equation in terms of the coefficients at CGL nodes,  $\tau_l$ , can be obtained by substituting Eq. (44) into Eq. (31) and (32).

For a generic matrix  $A(t)$ , the notation  $A_r$  denotes  $A(\tau_r)$ . Similarly  $X_r$  and  $\Lambda_r$  is also expressed in this way,  $r, l = 0, 1, \dots, N$ .

$$\sum_{l=0}^N V_{rl} X_l - T_r [A_r X_r - B_r R^{-1} (B_r)^T \Lambda_r] + B_r R^{-1} D^T \mu_r = h_r \quad (46)$$

$$\sum_{l=0}^N V_{rl} \boldsymbol{\Lambda}_l - T_r [\mathbf{Q} \mathbf{X}_r + (\mathbf{A}_r)^T \boldsymbol{\Lambda}_r] - \mathbf{C}^T \boldsymbol{\mu}_r = \mathbf{0} \quad (47)$$

$$\boldsymbol{\alpha}_r + \mathbf{C} \mathbf{X}_r - \mathbf{D} \mathbf{R}^{-1} (\mathbf{B}_r)^T \boldsymbol{\Lambda}_r - \frac{1}{T_r} \mathbf{D} \mathbf{R}^{-1} \mathbf{D}^T \boldsymbol{\mu}_r = -\boldsymbol{\nu}_r \quad (48)$$

The TPBVP with constraints defined by Eq. (46) is the discrete CGL pseudospectral approximation to the continuous-time TPBVP.

For simplicity, writing these equations in block matrix notation for  $\mathbf{X}^* = [(\mathbf{X}_0)^T, (\mathbf{X}_1)^T, \dots, (\mathbf{X}_N)^T]^T$ ,  $\boldsymbol{\Lambda}^* = [(\boldsymbol{\Lambda}_0)^T, (\boldsymbol{\Lambda}_1)^T, \dots, (\boldsymbol{\Lambda}_N)^T]^T$ ,

$$\mathbf{M}^* = [(\boldsymbol{\mu}_0)^T, (\boldsymbol{\mu}_1)^T, \dots, (\boldsymbol{\mu}_N)^T]^T, \mathbf{H}^* = [T(\tau_0), (\mathbf{h}_0)^T, \dots, T(\tau_N)(\mathbf{h}_N)^T]^T|_{n(N+1) \times 1}$$

we can obtain.

Eqs. (46)–(48) can also be conveniently rewritten into the form of

$$\mathcal{L} \boldsymbol{\chi} = \boldsymbol{\beta} \quad (49)$$

where  $\boldsymbol{\chi} = [\mathbf{X}^*; \boldsymbol{\Lambda}^*; \mathbf{M}^*]^T$ ,  $\boldsymbol{\beta} = [\mathbf{H}^*; \boldsymbol{\theta}]^T$ . The Box I in Fig. 4 indicates the specific form of  $\mathcal{L}$

$$\mathbf{L} \mathbf{X}^* + \mathbf{Y} \boldsymbol{\Lambda}^* + \mathbf{N} \mathbf{M}^* = -\boldsymbol{\nu} - \boldsymbol{\alpha} \quad (50)$$

where  $\mathbf{L}, \mathbf{Y}, \mathbf{N}$  are  $[n(N+1) \times n(N+1)]$  matrices whose  $ij$ th blocks are  $n \times n$  matrices defined by Eqs. (54)–(56). The state,  $\mathbf{X}^*$ , and costate,  $\boldsymbol{\Lambda}^*$ , are  $[n(N+1) \times 1]$  column vectors.

$$\boldsymbol{\mu}(\tau_l) \geq 0 \quad (51)$$

$$\boldsymbol{\alpha}(\tau_l) \geq 0 \quad (52)$$

$$\sum_{i=1}^N \boldsymbol{\mu}(\tau_i) \boldsymbol{\alpha}(\tau_i) = 0 \quad (53)$$

The resultant problem (51)–(53) is the mixed linear complementarity problem (MLCP). The MLCP can be easily handled using sophisticated schemes like Lemke's method, interior-point methods and noninterior continuation methods (Kanzow (1996)). Because the fact that concerned solvers can achieve high computational efficiency, the MLCP-based technique has been employed in a variety of real-time applications.

$$\mathbf{L} = \begin{bmatrix} C & & & \\ & C & & \\ & & \ddots & \\ & & & C \end{bmatrix} \quad (54)$$

$$\left[ \begin{array}{cccc|ccc|cc} V_{0,0} \mathbf{I}_n - T(\tau_0) \mathbf{A}_0 & V_{0,1} & \cdots & V_{0,N} & T(\tau_0) \mathbf{B}_0 \mathbf{R}^{-1} (\mathbf{B}_0)^T & & & \mathbf{B}_0 \mathbf{R}^{-1} \mathbf{D}^T \boldsymbol{\mu}_0 \\ V_{1,0} & V_{1,1} \mathbf{I}_n - T(\tau_1) \mathbf{A}_1 & \cdots & V_{1,N} & T(\tau_1) \mathbf{B}_1 \mathbf{R}^{-1} (\mathbf{B}_1)^T & & & \mathbf{B}_1 \mathbf{R}^{-1} \mathbf{D}^T \boldsymbol{\mu}_1 \\ \vdots & \vdots & \ddots & \vdots & \ddots & \ddots & & \ddots \\ V_{N,0} & V_{N,1} & \cdots & V_{N,N} \mathbf{I}_n - T(\tau_N) \mathbf{A}_N & & T(\tau_N) \mathbf{B}_N \mathbf{R}^{-1} (\mathbf{B}_N)^T & & \mathbf{B}_N \mathbf{R}^{-1} \mathbf{D}^T \boldsymbol{\mu}_N \\ \hline -T(\tau_0) \mathbf{Q} & & & & V_{0,0} \mathbf{I}_n - T(\tau_0) \mathbf{A}_0 & V_{0,1} & \cdots & V_{0,N} \\ & -T(\tau_1) \mathbf{Q} & & & V_{1,0} & V_{1,1} \mathbf{I}_n - T(\tau_1) \mathbf{A}_1 & \cdots & V_{1,N} \\ & & \ddots & & \vdots & \vdots & \ddots & \vdots \\ & & & -T(\tau_N) \mathbf{Q} & V_{N,0} & V_{N,1} & \cdots & V_{N,N} \mathbf{I}_n - T(\tau_N) \mathbf{A}_N \end{array} \right]$$

Fig. 4. BOX I.

$$Y = \begin{bmatrix} -\mathbf{D} \mathbf{R}^{-1} (\mathbf{B}_0)^T & & & \\ & -\mathbf{D} \mathbf{R}^{-1} (\mathbf{B}_1)^T & & \\ & & \ddots & \\ & & & -\mathbf{D} \mathbf{R}^{-1} (\mathbf{B}_N)^T \end{bmatrix} \quad (55)$$

$$N = \begin{bmatrix} -\frac{1}{T_0} \mathbf{D} \mathbf{R}^{-1} (\mathbf{D})^T & & & \\ & -\frac{1}{T_1} \mathbf{D} \mathbf{R}^{-1} (\mathbf{D})^T & & \\ & & \ddots & \\ & & & -\frac{1}{T_N} \mathbf{D} \mathbf{R}^{-1} (\mathbf{D})^T \end{bmatrix} \quad (56)$$

In the above,  $I_n$  and  $0_n$  are the  $n \times n$  identity and zero matrices, respectively. The goal is to solve Eq. (49) and Eq. (50) subject to the boundary conditions Eq. (37). The matrix form of these equations can be expressed by Eq. (57).

$$\begin{bmatrix} \mathcal{L} \\ \mathcal{P} \\ \mathcal{A} \end{bmatrix} \boldsymbol{\chi} = \begin{bmatrix} \mathbf{H}^* \\ \boldsymbol{\theta} \\ -\boldsymbol{\nu} - \boldsymbol{\alpha} \end{bmatrix} \quad (57)$$

where  $\mathcal{P} = [\mathbf{P}_1, \mathbf{P}_2, \mathbf{P}_3]$ ,  $\mathcal{A} = [\mathbf{L}, \mathbf{Y}, \mathbf{N}]$  And  $n \times n(N+1)$  matrices  $\mathbf{P}_1, \mathbf{P}_2$  and  $\mathbf{P}_3$  are  $\mathbf{P}_1 = [0_n, \dots, 0_n, \mathbf{P}], \mathbf{P}_2 = [0_n, \dots, 0_n, -\mathbf{I}_n], \mathbf{P}_3 = \mathbf{0}$ . Obviously, Eq. (57) is shaped like  $Ax = b$ .  $x = A \setminus b$ , the operator denotes the least squares solution. Thus, we can obtain the states and costates by solving Eq. (57). The electrostatic forces and torques at CGL points are also solved from Eq. (26).

**Remark 3.** (Convergence and stability analysis) As a matter of fact, the convergence of the ICPM is determined by the employed quasi-linearization technique and the Chebyshev polynomials, which has a fast rate of convergence compared with other ultra-spherical polynomials (Fox and Parker (1968), Jaddu (2002)), in combination with the quasi-linearization. The converging to the optimal solution of quasi-linearization techniques has also been discussed (Bellman and Quasilinearization (1965), Jaddu (1999), Jaddu (2002)).

Because the relative dynamics for TM is handled by quasi-linearization and discretized with a sampling period  $T$ . In analyzing the stability characteristics of model predictive control, an approach that has received substantial attention is multiple Lyapunov functions (Yan et al.

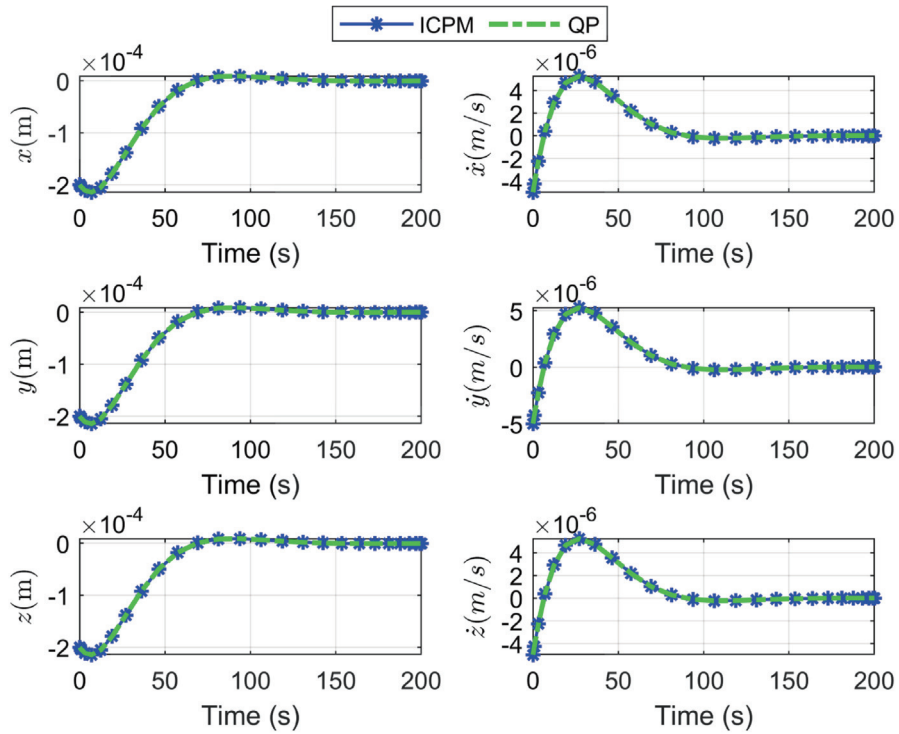


Fig. 5. The relative position.

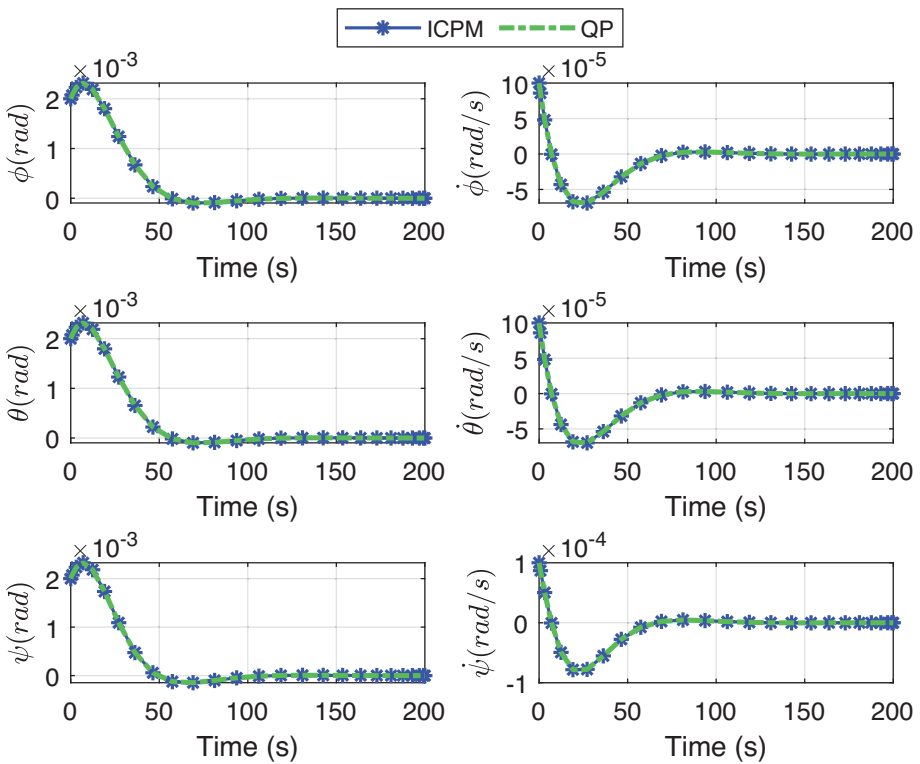


Fig. 6. The relative attitude.

(2020), Bryson and Ho (2018)). The specific proof process is given in Maciejowski (2002).

#### 4. Simulation results

The feasibility and performance of the proposed control structure are evaluated in numerical simulations. The general optimal open-loop control is introduced in Section 4.1. Section 4.2 focuses on the closed-loop control on TM capture mode tests. Comparison against frequently-used approaches is also discussed. All the calculations are performed on a personal computer with Core i5-8500 CPU (3.00 GHz) processor using 16.0 GB RAM. The resultant random disturbances, control requirements and system parameters are defined in Appendix.

##### 4.1. Optimal algorithm test

The initial state  $x_0 = [2 \times 10^{-4}, 5 \times 10^{-6}, 2 \times 10^{-4}, 5 \times 10^{-6}, 2 \times 10^{-4}, 5 \times 10^{-6}, 2 \times 10^{-3}, 1 \times 10^{-4}, 2 \times 10^{-3}, 1 \times 10^{-4}, 2 \times 10^{-3}, 1 \times 10^{-4}]$  is set to the maximum amplitude of permitted scope in Table 7. The number of collocation points is 26. The optimization time is 200s. The mass of TM is 2.45kg.  $J_{ix}, J_{iy}, J_{iz} = 7.0 \times 10^{-4}$ . By properly selecting the release points, the relative motion and the control requirement can be reduced effectively. According to (Lian et al. (2021b)), the ideal release point of the test

mass 1 (TM1) and test mass 2 (TM2) are  $(0.3m, 0, 0)$  and  $(-0.3m, 0, 0)$  in Oxyz, respectively. The constraints for state and input are shown in Appendix.

Comparisons are drawn with the computational load of QP solver (Cannon et al. (2008)) and ICPM for state and input constraints. The translation and attitude of TM are commanded to meet the accuracy requirements in Table 8 by using the ICPM with input and state constraints. The relative translation and attitude of TM1 are displayed in

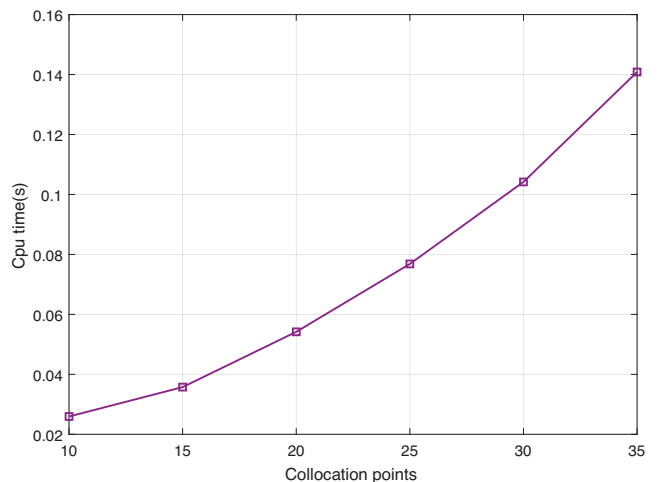


Fig. 8. Calculation time.

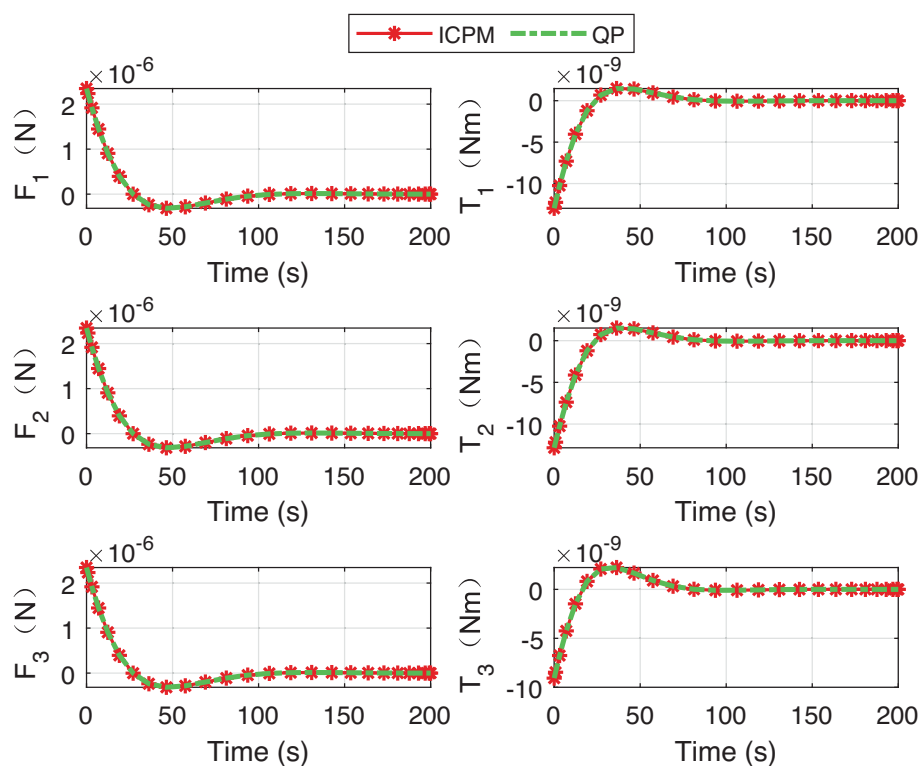


Fig. 7. The control force of ICPM.

Table 1  
Calculation time for ICPM and QP.

Simulation Number	1	2	3	...	15000	Average Value
ICPM(N = 26)	0.0823s	0.0822s	0.0819s	...	0.0821s	0.0821s
QP	0.3305s	0.3300s	0.3303s	...	0.3300s	0.3302s

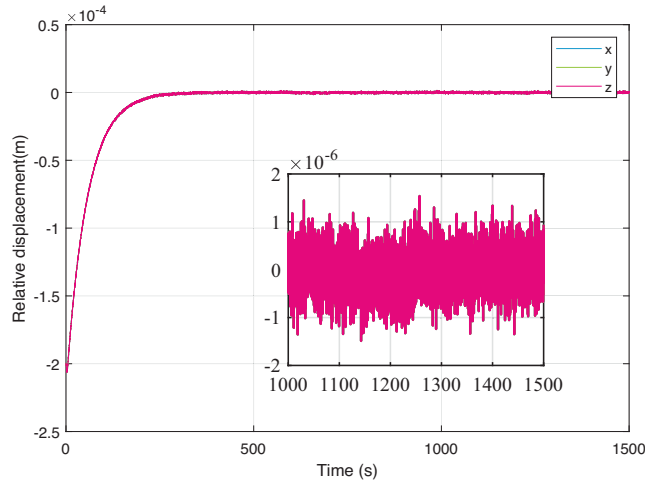


Fig. 9. The relative position (SMC).

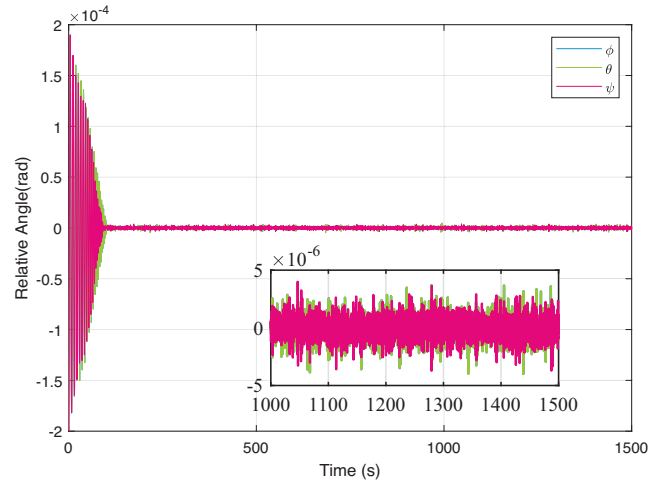


Fig. 11. The relative attitude between (SMC).

Fig. 5–Fig. 6 with the distribution of CGL collocation points highlighted in an asterisk and QP highlighted in a dotted line. The solutions of controllers are also shown in Fig. 7. The system stabilization takes approximately 100s.

According to (Li and Peng (2016)), the numerical results of ICPM are almost consistent with the expected optimal state and control trajectories, thus verifying the validity of ICPM. The feasibility is also tested in this section. The

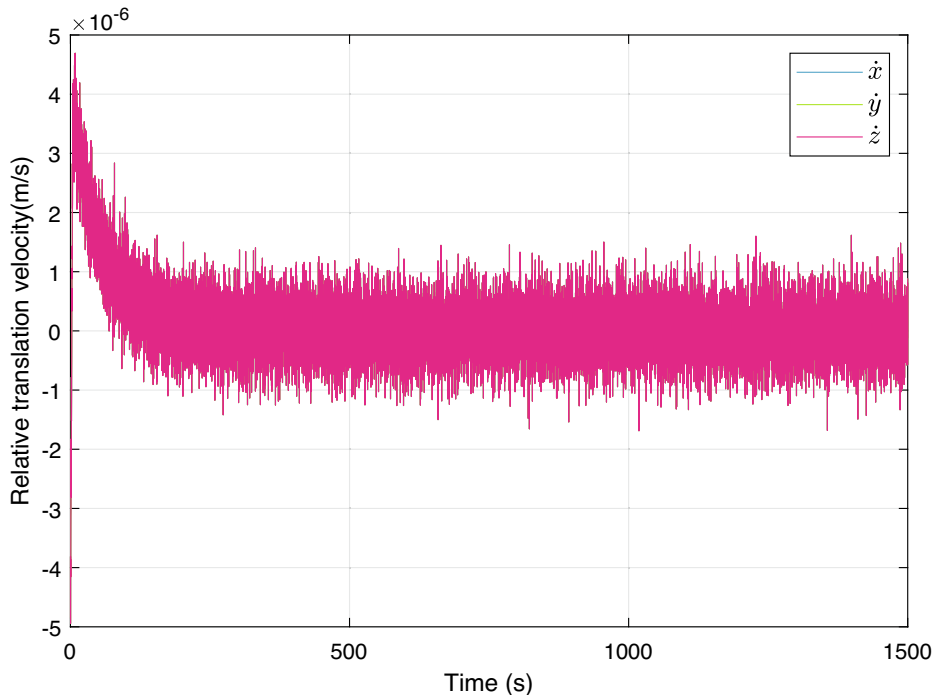


Fig. 10. The relative translation velocity (SMC).

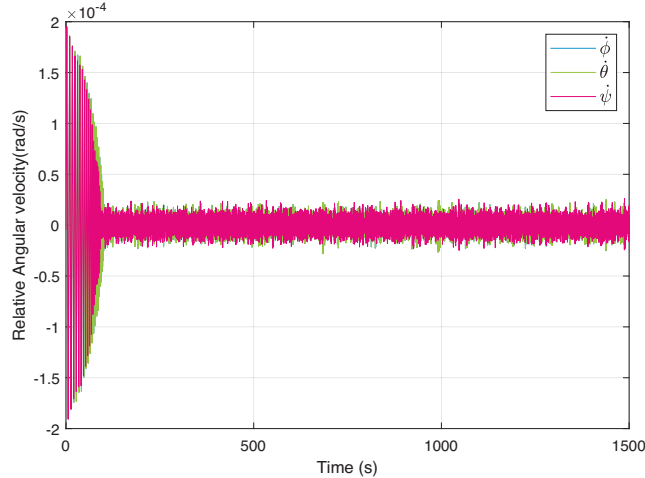


Fig. 12. The relative angular velocity (SMC).

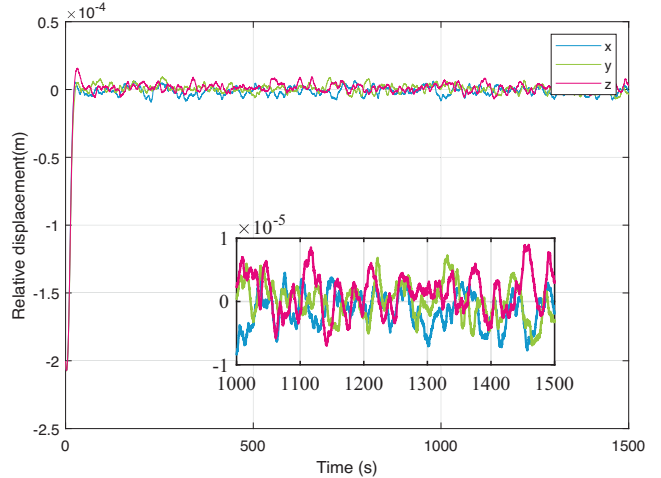


Fig. 15. The relative position (custom MPC).

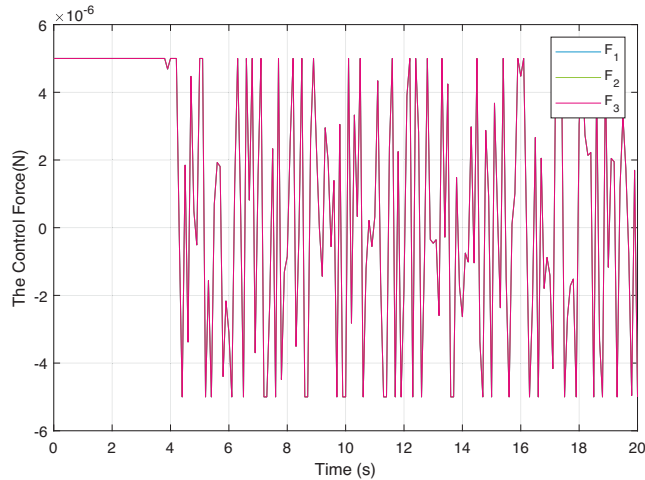


Fig. 13. The control force (SMC).

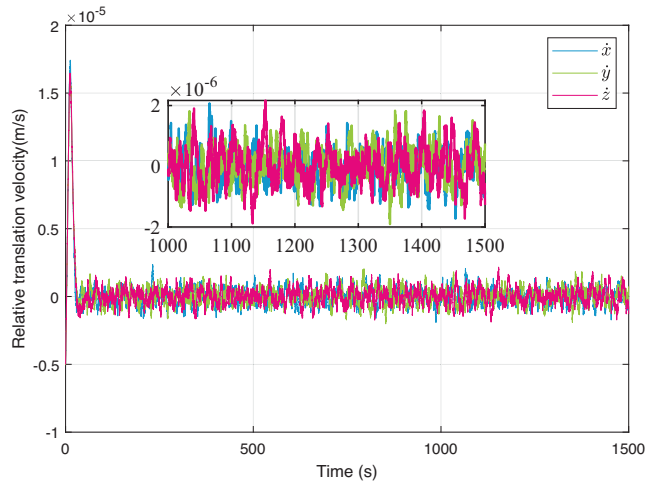


Fig. 16. The relative translation velocity (custom MPC).

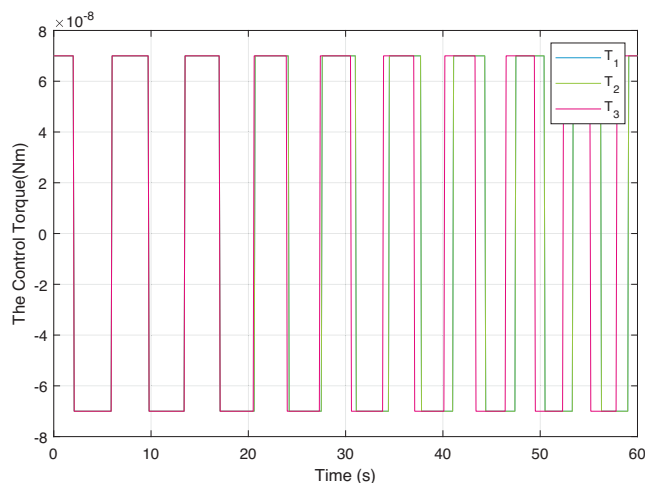


Fig. 14. The control torque (SMC).

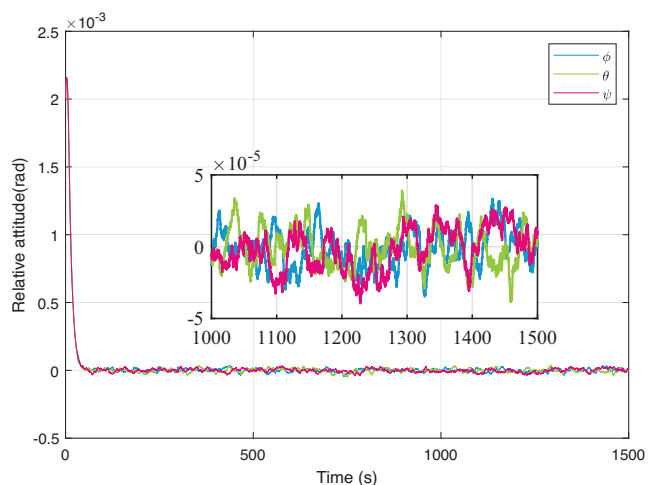


Fig. 17. The relative attitude (custom MPC).

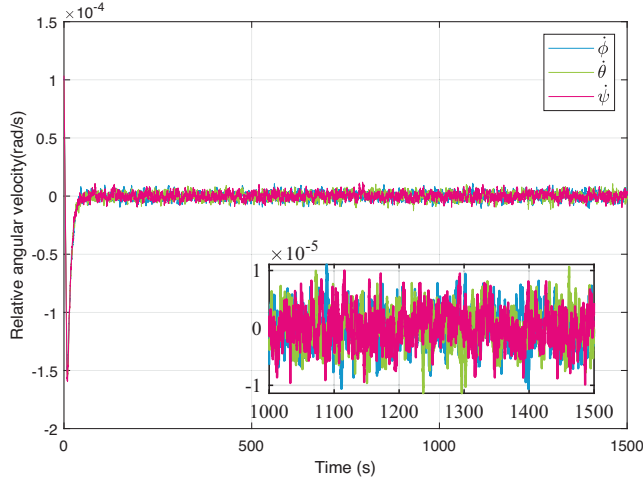


Fig. 18. The relative angular velocity (custom MPC).

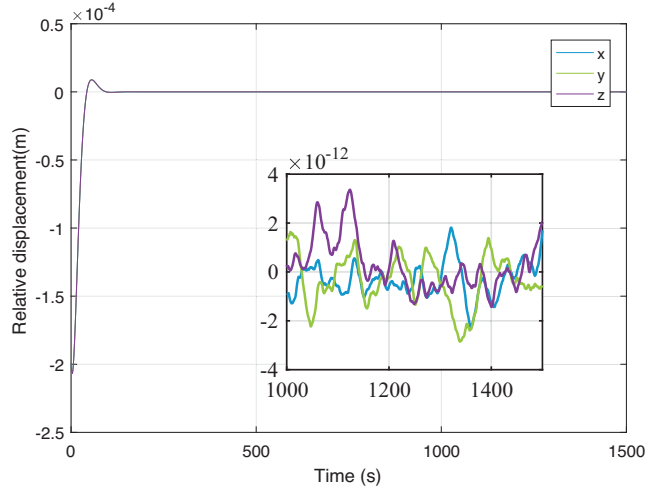


Fig. 21. Relative position (NHMPC).

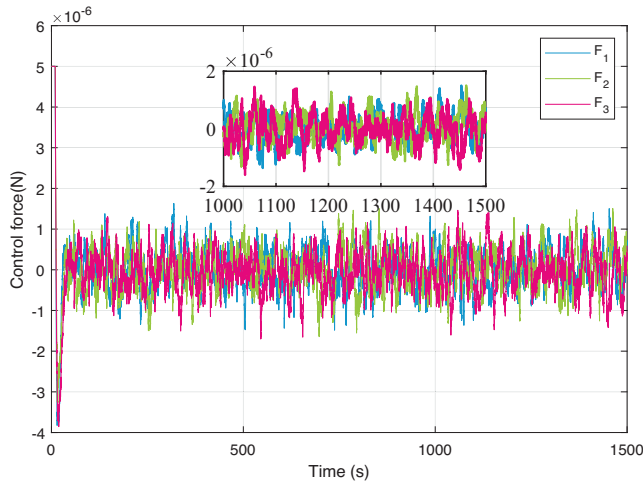


Fig. 19. The control force (custom MPC).

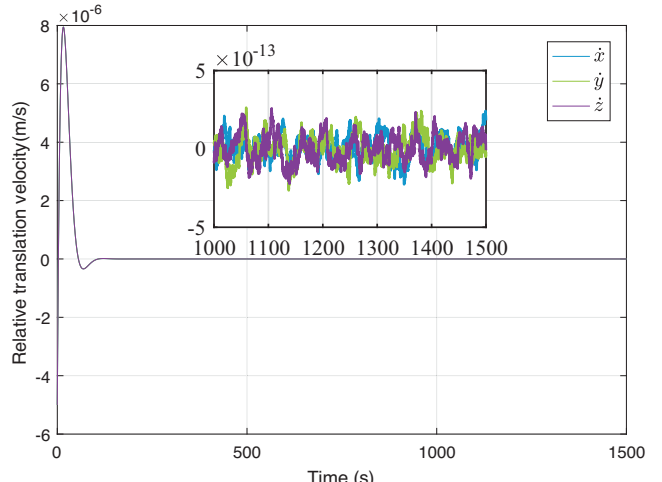


Fig. 22. Relative translation velocity (NHMPC).

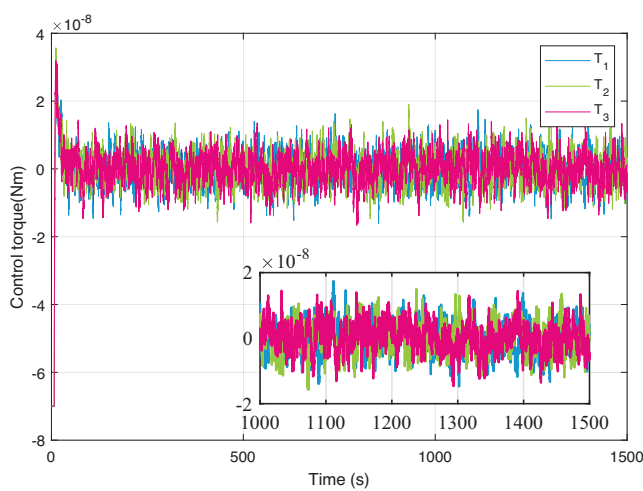


Fig. 20. The control torque (custom MPC).

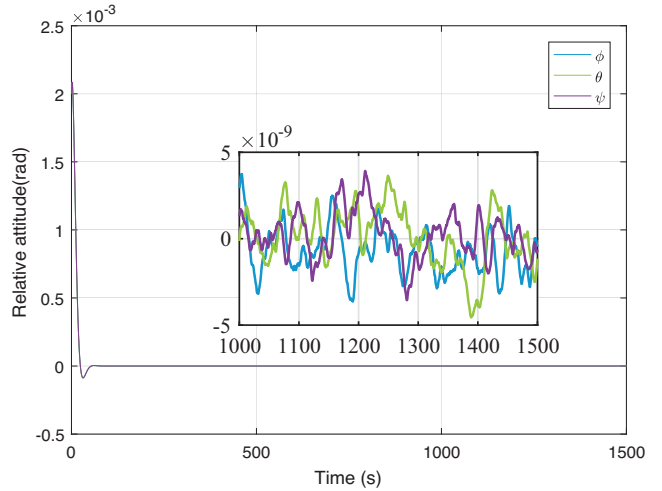


Fig. 23. The relative attitude between TM and cavity (NHMPC).

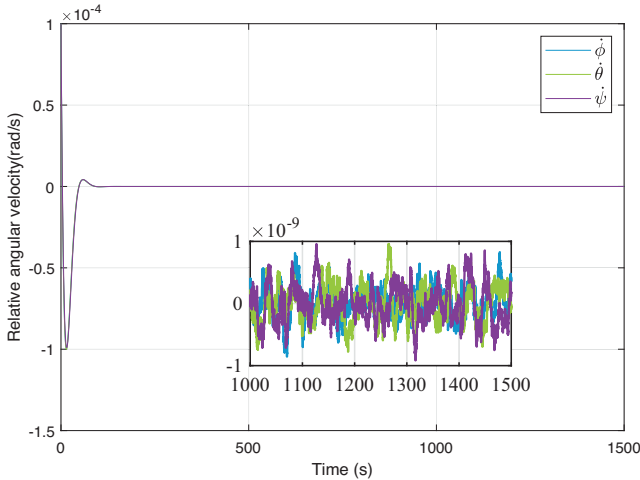


Fig. 24. The relative angular velocity between TM and cavity (NHMPC).

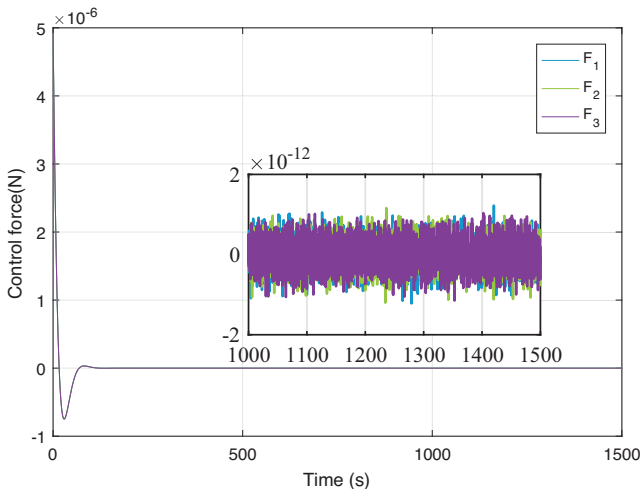


Fig. 25. The control force (NHMPC).

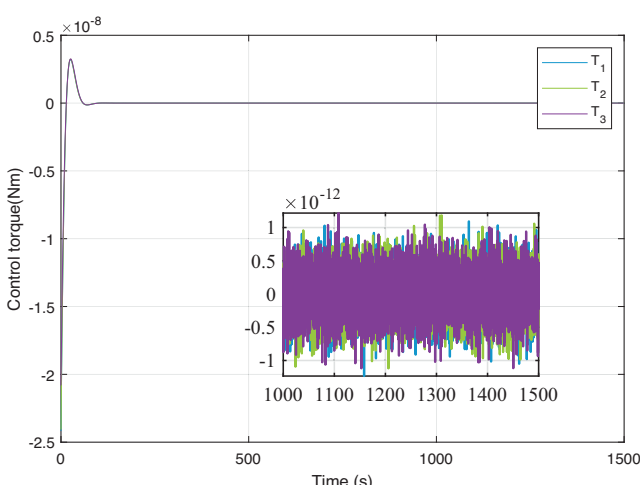


Fig. 26. The control torque (NHMPC).

relative translation and angle trajectories converge to zero at about 90s in Fig. 5 and Fig. 6, which demonstrates the TM is captured with the considering cost function. The control inputs without noises shown in Fig. 7 are stable and change slowly. Moreover, it is also clear to see that the ICPM in the designed NHMPC and the QP method generate close solutions. This means that the ICPM solution accuracy used in NHMPC is well enough. For the numerical convergence of ICPM at the collocation points, since the open-loop optimal trajectory is stable, the numerical value must be convergent.

Concerning efficiency of the proposed MPC framework, the different number of collocation points is well experimental in Fig. 8. Although the calculation time increases with the increasing number of collocation points, which means the performance of real-time gets worse, the calculation time is still within 0.1s when the collocation points are not more than 29. Note that the number of points does not need too much. According to points selection experience in the indirect pseudospectral method, generally a few can achieve the required accuracy. In this paper, 10 to 26 points selected to calculate is enough. The CPU times in Fig. 8 are the average amplitude of 15000 simulations considering the relative translation and attitude simultaneously. To ensure approximate accuracy, at least 7 points are selected. The collocation points are set to 26 in Fig. 5–Fig. 7. Furthermore, to compare their computational efficiency, the ICPM and QP are implemented 15000 times. The computational times are presented in Table 1. The average calculation time of 15000 simulations for displacement and attitude stabilization is 0.0821s, while the QP in custom MPC requires 0.3302s to complete the numerical calculation. The numerical results demonstrate that the developed NHMPC can generate an accurate solution with a lower computational burden. This conclusion allows the assumption that the solving speed of ICPM can satisfy the control cycle requirements of drag-free satellites in engineering.

#### 4.2. Close-loop control test

Sliding mode control (SMC) is a major method for TM capture mode in the LISA Pathfinder mission (Schleicher et al. (2018), Montemurro et al. (2006), Montemurro et al. (2007)), which has strong robustness to handle the noises and uncertainties. Because optimality is not considered, the performance is conservative. Although the traditional MPC method (Vidano et al. (2022)) has both robustness and optimality, it is difficult to calculate with time-consuming and to apply in engineering, especially in the case of constraints. This phenomenon is also at work in SubSection 4.2. In addition, the traditional MPC parameter tuning process is tedious and difficult to obtain the ideal curve which is also needed to overcome. To further evaluate the performance of the developed NHMPC method under input and state constraints, a custom MPC based QP which is similar to (Vidano et al. (2022)) and an SMC like (Lian et al. (2022)) are implemented.

Table 2  
Cost function parameters.

	$q_t$	$r_t$	$q_a$	$r_a$
Traditional MPC	$3 \times 10^2$	$1 \times 10^6$	5	$2 \times 10^9$
NHMPC	$1 \times 10^4$	$1 \times 10^6$	$1 \times 10^2$	$5 \times 10^9$

To test control system behavior during the stabilization for TM capture, simulations for the proposed method, sliding mode control (SMC) method and traditional MPC method are performed and compared in Fig. 9–26. For clarity of comparison, the simulation times are set to 1500s. The prediction horizon is  $T_1 = 200$ s, and the sample time is  $T = 0.1$ s. The control horizon is 0.1s. To assess the influence of noises on the relative TM displacement and attitude, various noise sources have been simultaneously added to the simulator. This simulation determines the constant disturbances, actuation and sensing noises according to the values reported in the Appendix. The value of constant disturbance  $d_{DC}$  is set to  $5 \times 10^{-8}$ . The parameters for NHMPC and the traditional MPC method are shown in (58). While the numerical results strongly depend on the respective tuning, some fundamental differences among the three approaches can still be observed. The state and control trajectories solved by SMC are displayed in Fig. 9–14. The solving results for traditional MPC and NHMPC are shown in Fig. 15–20 and Fig. 21–26, respectively.

$$Q = \begin{bmatrix} q_t \mathbf{I}_6 & \mathbf{O}_6 \\ \mathbf{O}_6 & q_a \mathbf{I}_6 \end{bmatrix}, R = \begin{bmatrix} r_t \mathbf{I}_6 & \mathbf{O}_6 \\ \mathbf{O}_6 & r_a \mathbf{I}_6 \end{bmatrix} \quad (58)$$

where  $q_t, r_t, q_a$  and  $r_a$  are defined in Table 2

At the beginning of the simulation, the test mass is quickly escaping from the cage center due to the bad initial conditions. As shown in the below picture, the three methods can make states tend to be stable and meet the saturation constraint requirements in Appendix, which represents that the state and control do not violate the prescribed con-

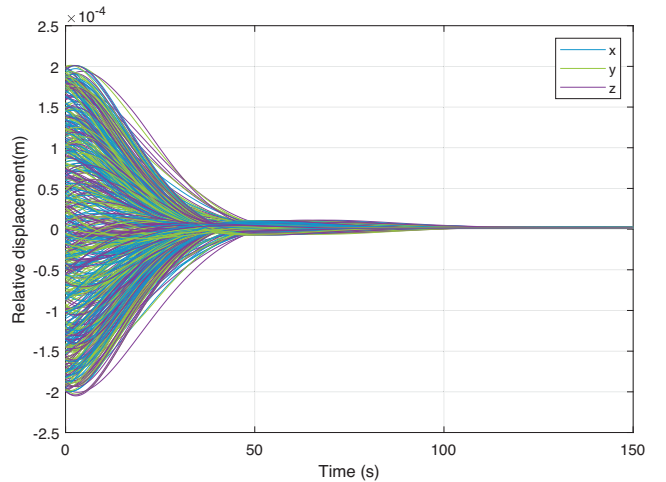


Fig. 27. The relative position in Monte-Carlo.

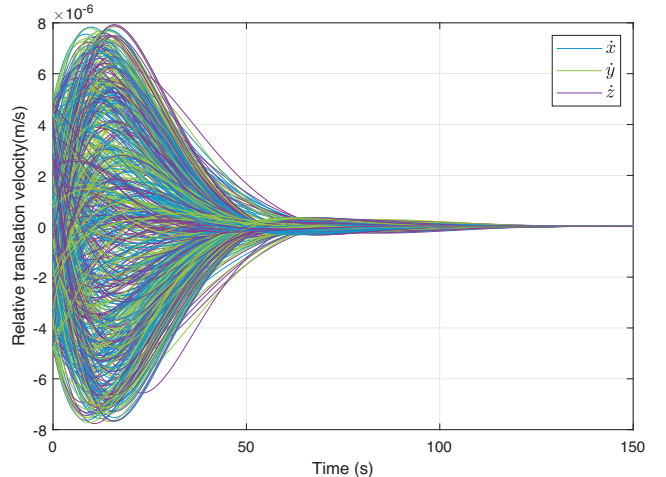


Fig. 28. The relative translation velocity in Monte-Carlo.

Table 3  
Performance comparison.

	Stabilization time(s)			Error accuracy			Overshoot		
	SMC	Traditional MPC	NHMPC	SMC	Traditional MPC	NHMPC	SMC	Traditional MPC	NHMPC
Translation(m)	272	106	110	$1.5 \times 10^{-6}$	$9.2 \times 10^{-6}$	$3.5 \times 10^{-12}$	0	$1.5 \times 10^{-5}$	$1.5 \times 10^{-5}$
Translation velocity(m/s)	272	106	110	$1.5 \times 10^{-6}$	$2.1 \times 10^{-6}$	$2.8 \times 10^{-13}$	0	$1.7 \times 10^{-5}$	$8.0 \times 10^{-6}$
Angle(rad)	112	87	85	$4.0 \times 10^{-6}$	$4.0 \times 10^{-5}$	$4.0 \times 10^{-9}$	$2.0 \times 10^{-4}$	$2.0 \times 10^{-4}$	$1.0 \times 10^{-4}$
Angular velocity(rad/s)	112	87	85	$2.0 \times 10^{-5}$	$1.0 \times 10^{-5}$	$9.0 \times 10^{-10}$	$2.0 \times 10^{-4}$	$1.6 \times 10^{-4}$	$1.4 \times 10^{-5}$

Table 4  
The control accuracy.

Force accuracy(N)			Torque accuracy(Nm)		
SMC	Traditional MPC	NHMPC	SMC	Traditional MPC	NHMPC
$5.0 \times 10^{-6}$	$1.5 \times 10^{-6}$	$8.0 \times 10^{-13}$	$7.0 \times 10^{-8}$	$1.9 \times 10^{-8}$	$9.0 \times 10^{-13}$

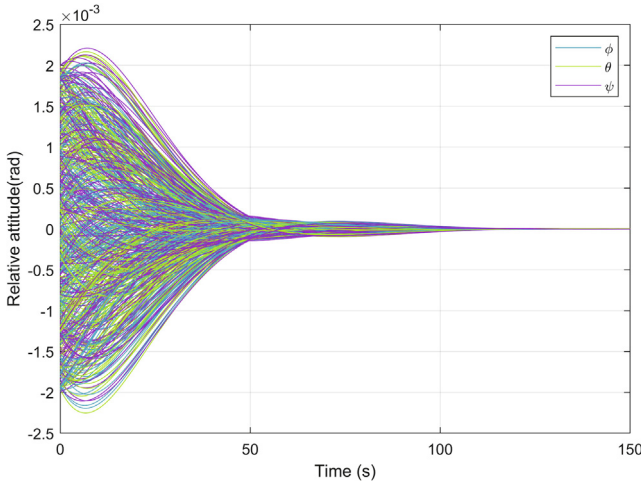


Fig. 29. The relative attitude in Monte-Carlo.

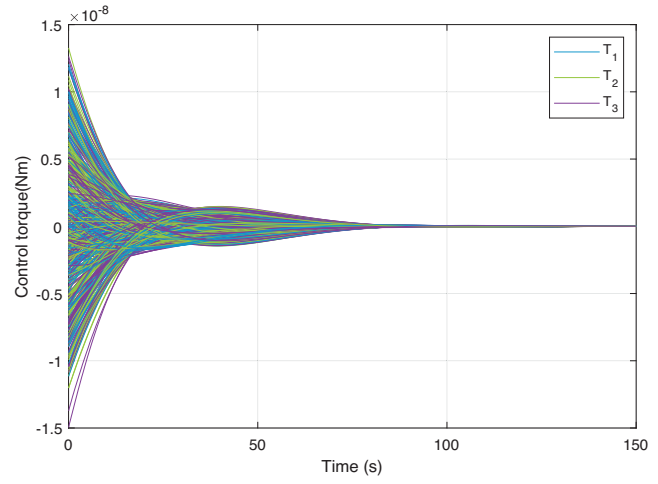


Fig. 32. The control torque in Monte-Carlo.

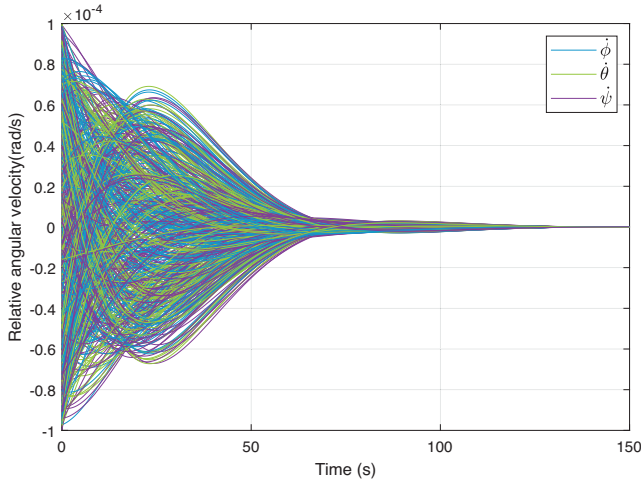


Fig. 30. The relative angular velocity in Monte-Carlo.

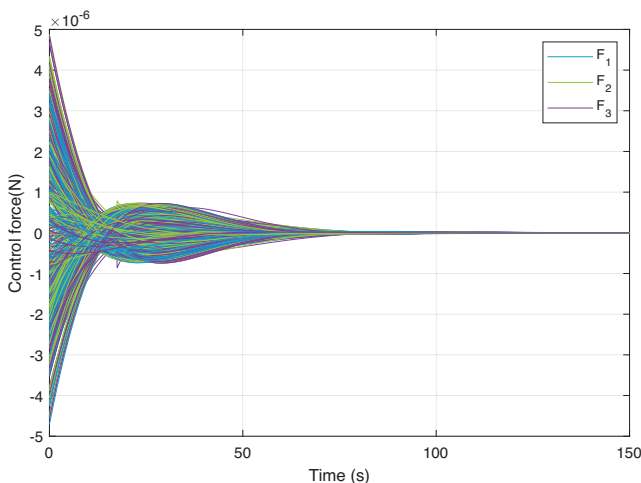


Fig. 31. The control force in Monte-Carlo.

straints (15) about the command and state saturations. **Table 3 and 4** show the specific performance parameters of the three methods under an average of 10 simulations. It can be seen that although the SMC method can stabilize TM to the center of the electrode cage and meet the requirements of control error, the dynamic process jitter is severe. Hereby, the MPC applies relatively large forces and torques to minimize the output error. The traditional MPC can reduce the high frequency jitter. It can achieve almost the same control precision as SMC and calm down faster than the SMC method when using smaller control torque than SMC. However, due to the difficulty of parameter setting, the control precision of the attitude loop is slightly beyond the specified range in this simulation.

The simulation results with random disturbances further demonstrate the robustness of the designed MPC method. The NHMPC significantly improves the control accuracy by about 3 to 6 orders of magnitude compared to SMC and traditional MPC, and the stabilization time is similar to that of conventional MPC methods. This means that the designed MPC method with random disturbances has a better control effect compared to the other two methods. And the developed NHMPC method can generate an accurate solution with a lower computational burden. More importantly, due to the characteristics of ICPM of fast computing speed and high solving accuracy, the real-time performance of MPC is improved. Through the experiment of the current numerical simulation stage, it is feasible to be used in practical engineering.

#### 4.3. Monte-Carlo test

In this section, a Monte-Carlo (MC) analysis is conducted to get more confidence in the robustness of NHMPC. 500 simulations have been done, using the same parameters and disturbance distribution as the previous simulation. The simulation time is set to 150s. Regarding

Table 5  
The performance in Monte-Carlo.

	Max stabilization time	Max overshoot	Error accuracy range
Translation	119s	$1.55 \times 10^{-5}$ m	$\pm 4.33 \times 10^{-11}$ m
Translation velocity	119s	$8.28 \times 10^{-6}$ m/s	$\pm 2.12 \times 10^{-12}$ m/s
Angle	112s	$1.20 \times 10^{-4}$ rad	$\pm 5.79 \times 10^{-9}$ rad
Angular velocity	131s	$7.1 \times 10^{-5}$ rad/s	$\pm 2.92 \times 10^{-9}$ rad/s
Force	91s	$5.1 \times 10^{-7}$ N	$\pm 1.97 \times 10^{-12}$ N
Torque	87s	$1.90 \times 10^{-9}$ Nm	$\pm 2.88 \times 10^{-12}$ Nm

the disturbances, a Monte-Carlo campaign is performed using a simulation environment which includes solar pressure noises, constant disturbances, local environment noises, actuation and sensing noises of the electrostatic suspension. The initial conditions are randomly chosen from the following variation range.

$$\begin{aligned} |r_{ix0}|, |r_{iy0}|, |r_{iz0}| &\leq 2 \times 10^{-4} \\ |\dot{r}_{ix0}|, |\dot{r}_{iy0}|, |\dot{r}_{iz0}| &\leq 5 \times 10^{-6} \\ |\varphi_{i0}|, |\theta_{i0}|, |\psi_{i0}| &\leq 2 \times 10^{-3} \\ |\dot{\varphi}_{i0}|, |\dot{\theta}_{i0}|, |\dot{\psi}_{i0}| &\leq 1 \times 10^{-4} \end{aligned} \quad (59)$$

Constant disturbances act on the TM and inertia coefficients are randomly initialized from the following variation range.

$$|d_{DC}| \leq 5 \times 10^{-8}, |J_{ix}|, |J_{iy}|, |J_{iz}| \leq 7.1 \times 10^{-4}$$

Fig. 27–30 show the displacement and attitude trajectories with the parameter, initial condition and noise uncertainties under the MC test. The forces and torques are also shown in Fig. 31 and Fig. 32. The statistic result of MC is summarized in Table 5, where the advantages and robustness of the NHMPC can be seen. In 100% of the scenarios simulated, the NHMPC controller is able to achieve stability and meet the performance required under the different parameter uncertainties. The maximum stability time of the NHMPC is slightly longer than the SMC and custom MPC in Table 3, while the maximum overshoot of the NHMPC is smaller than that of the other two methods. This fact is appreciated in Fig. 27–32 where is plotted the state and input trajectories, in the cases when the controllers can achieve TM capture without constraints violations. This phenomenon not only verifies the robustness of NHMPC but also shows good control performance. Note that the results of NHMPC are constantly oscillating and converging, and the control accuracy can reach the order of  $10^{-9} - 10^{-12}$ , which can be seen from the trajectory trend of Section 4.2.

While the test masses are released and controlled, the spacecraft has to keep the reference attitude compensating for the solar pressure torque and the internal reaction forces/torques of the two electrostatic suspensions. Control methods such as QFT, mixed sensitivity and EMC, etc., can effectively control the attitude of the satellite body. Therefore, this paper will not repeat this aspect.

## 5. Conclusion

This paper presented the test mass capture control with robustness and optimality for drag-free satellites. Using an ICPM, the optimal module computes optimal trajectories of states and control inputs, which is an open control loop. Then, the closed-loop control is established by nonlinear MPC to achieve the TM capture. The proposed MPC framework allows one to trade off computation time vs. performance. Numerical experiments have verified the success of the proposed control structure. The validity and efficiency of the proposed control were also evaluated and confirmed in experiments. Successful TM capture was achieved in the presence of measure noises, actuation noises and dynamic noises, showing the NHMPC's capabilities. Simulation results for comparison with a representative state-of-the-art approach were provided and showed that the proposed NHMPC for TM capture outperforms current mainstream approaches.

## Declaration of Competing Interest

The authors declare that they have no known competing financial interests or personal relationships that could have appeared to influence the work reported in this paper.

## Appendix A

The requirements are defined in (Trobbiani (2014)), which are elaborated in this section.

Maximum linear displacement overshoot:  $< 1\text{mm}$ ;  
Maximum rotation overshoot:  $< 10\text{mrad}$ ;  
Maximum control force:  $< 5 \times 10^{-6}\text{N}$ ;  
Maximum control torque:  $< 7 \times 10^{-8}\text{Nm}$ .

Other requirements and parameters are shown in the Table 6–9.

Table 6  
The orbit parameters for numerical simulations.

Parameters	Values
Standard gravitational parameter $\mu$	$3.9860 \times 10^{14} \text{ m}^3/\text{s}^2$
Semimajor axes $a$	9995.5723 km
Initial true anomaly $f_0$	61.3296°
Eccentricity $e$	0.0004300
Argument of perigee	346.5528°
RAAN	211.6003°
Inclination $i$	74.5362°

Table 7

The initial state requirements of TM (release requirements).

States	Values
Offset along $x, y$ , and $z$	$\pm 200 \mu\text{m}$
Linear velocity along $x, y$ , and $z$	$\pm 5 \mu\text{m/s}$
Angle around $x, y$ , and $z$	$\pm 2 \text{ mrad}$
Angular rate around $x, y$ , and $z$	$\pm 100 \mu\text{rad/s}$

Table 8

Control accuracy requirements (transition to steady state).

Test mass states	Control accuracy
Linear velocity, relative to test mass housing	$< 1 \cdot 10^{-6} \text{ m/s}$
Rotational rate, relative to test mass housing	$< 1 \cdot 10^{-5} \text{ rad/s}$
Displacement with respect to test mass housing	$< 25 \mu\text{m}$
Attitude with respect to test mass housing	$< 100 \mu\text{rad}$

Table 9

Noise variances (White noises).

Axis	Process noise variances	Measurement noise variances	Actuation noise variances
x	$1.641 \cdot 10^{-20} \text{ m}^2/\text{s}^4$	$1.679 \cdot 10^{-13} \text{ m}^2$	$1 \cdot 10^{-24} \text{ N}^2$
y	$6.247 \cdot 10^{-20} \text{ m}^2/\text{s}^4$	$1.380 \cdot 10^{-13} \text{ m}^2$	$1 \cdot 10^{-24} \text{ N}^2$
z	$2.605 \cdot 10^{-29} \text{ m}^2/\text{s}^4$	$3.690 \cdot 10^{-13} \text{ m}^2$	$1 \cdot 10^{-24} \text{ N}^2$
$\phi$	$1.216 \cdot 10^{-17} \text{ rad}^2/\text{s}^4$	$5.720 \cdot 10^{-9} \text{ rad}^2$	$1 \cdot 10^{-24} \text{ N}^2 \cdot \text{m}^2$
$\theta$	$4.863 \cdot 10^{-17} \text{ rad}^2/\text{s}^4$	$1.589 \cdot 10^{-8} \text{ rad}^2$	$1 \cdot 10^{-24} \text{ N}^2 \cdot \text{m}^2$
$\psi$	$1.66 \cdot 10^{-18} \text{ rad}^2/\text{s}^4$	$1.345 \cdot 10^{-8} \text{ rad}^2$	$1 \cdot 10^{-24} \text{ N}^2 \cdot \text{m}^2$

## References

- Allenspach, M., Ducard, G.J.J., 2021. Nonlinear model predictive control and guidance for a propeller-tilting hybrid unmanned air vehicle. *Automatica* 132, 109790.
- Armano, M., Audley, H., Auger, G., et al., 2016. Sub-femto-g free fall for space-based gravitational wave observatories: Lisa pathfinder results. *Phys. Rev. Lett.* 116 (23), 231101.
- Armano, M., Audley, H., Auger, G., et al., 2015. The lisa pathfinder mission. *Journal of Physics: Conference Series*, vol. 610. IOP Publishing, p. 012005.
- Bellman, R.E., Quasilinearization, R.K., 1965. *Nonlinear Boundary-Value Problems*. American Elsevier Publishing Co., Inc, New York.
- Bortoluzzi, D., Armano, M., Audley, H. et al., 2016. Injection of a body into a geodesic: Lessons learnt from the lisa pathfinder case. In: 43rd Aerospace Mechanisms Symposium.
- Bortoluzzi, D., Vignotto, D., Dalla Ricca, E., et al., 2021. Investigation of the in-flight anomalies of the lisa pathfinder test mass release mechanism. *Adv. Space Res.* 68 (6), 2600–2615.
- Bryson, A.E., Ho, Y.-C., 2018. *Applied Optimal Control: Optimization, Estimation, and Control*. Routledge.
- Cannon, M., Liao, W., Kouvaritakis, B., 2008. Efficient mpc optimization using pontryagin's minimum principle. *Int. J. Robust Nonlinear Control*: IFAC-Affil. J. 18 (8), 831–844.
- Chai, R., Savvaris, A., Tsourdos, A., et al., 2018. Optimal tracking guidance for aeroassisted spacecraft reconnaissance mission based on receding horizon control. *IEEE Trans. Aerosp. Electron. Syst.* 54 (4), 1575–1588.
- Deng, H., Ohtsuka, T., 2018. A highly parallelizable newton-type method for nonlinear model predictive control. *IFAC-PapersOnLine* 51 (20), 349–355.
- Deng, H., Ohtsuka, T., 2019. A parallel newton-type method for nonlinear model predictive control. *Automatica* 109, 108560.
- Deng, H., Ohtsuka, T., 2022. Parnmpc—a parallel optimisation toolkit for real-time nonlinear model predictive control. *Int. J. Control* 95 (2), 390–405.
- Fox, L., Parker, I.B., 1968. *Chebyshev Polynomials in Numerical Analysis*. Oxford Mathematical Handbook, London.
- Gong, Y., Luo, J., Wang, B., 2021. Concepts and status of chinese space gravitational wave detection projects. *Nature Astronomy* 5 (9), 881–889.
- Jaddu, H., 1999. Computational method based on state parametrization for solving constrained nonlinear optimal control problems. *Int. J. Syst. Sci.* 30 (3), 275–282.
- Jaddu, H., 2002. Direct solution of nonlinear optimal control problems using quasilinearization and chebyshev polynomials. *J. Franklin Inst.* 339 (4–5), 479–498.
- Kanzow, C., 1996. Some noninterior continuation methods for linear complementarity problems. *SIAM J. Matrix Anal. Appl.* 17 (4), 851–868.
- Lemos, J.M., 2010. Nonlinear receding horizon control based on pontryagin optimum principle. *IFAC Proc. Vol.* 43 (14), 1069–1074.
- Li, D.-T., Wu, A.-G., Li, P., 2020. Nonlinear model predictive control for spacecraft attitude tracking with kalman filter. In: 2020 Chinese Automation Congress (CAC). IEEE, pp. 3389–3394.
- Li, M., Peng, H., 2016. Solutions of nonlinear constrained optimal control problems using quasilinearization and variational pseudospectral methods. *ISA Trans.* 62, 177–192.
- Lian, X., Zhang, J., Chang, L., et al., 2022. Test mass capture for drag-free satellite based on rbf neural network adaptive sliding mode control. *Adv. Space Res.* 69 (2), 1205–1219.
- Lian, X., Zhang, J., Lu, L., et al., 2021a. Frequency separation control for drag-free satellite with frequency-domain constraints. *IEEE Trans. Aerosp. Electron. Syst.* 57 (6), 4085–4096.
- Lian, X., Zhang, J., Yang, J., et al., 2021b. The determination for ideal release point of test masses in drag-free satellites for the detection of gravitational waves. *Adv. Space Res.* 67 (2), 824–833.
- Maciejowski, J.M., 2002. *Predictive Control: with Constraints*. Pearson Education.
- Mayne, D.Q., Rawlings, J.B., Rao, C.V., et al., 2000. Constrained model predictive control: Stability and optimality. *Automatica* 36 (6), 789–814.
- Montemurro, F., Fichter, W., Schlotterer, M., 2007. Sliding mode technique applied to test mass suspension control. *IFAC Proc. Vol.* 40 (7), 627–632.
- Montemurro, F., Fichter, W., Schlotterer, M., et al., 2006. Control design of the test mass release mode for the lisa pathfinder mission. *AIP Conference Proceedings*, vol. 873. American Institute of Physics, pp. 583–587.
- Morgan, D., Chung, S.-J., Hadaegh, F.Y., 2014. Model predictive control of swarms of spacecraft using sequential convex programming. *J. Guidance Control Dyn.* 37 (6), 1725–1740.
- Pagone, M., Boggio, M., Novara, C., et al., 2022. A penalty function approach to constrained pontryagin-based nonlinear model predictive control. In: 2022 IEEE 61st Conference on Decision and Control (CDC). IEEE, pp. 3705–3710.
- Palanki, S., Kravaris, C., Wang, H.Y., 1993. Synthesis of state feedback laws for end-point optimization in batch processes. *Chem. Eng. Sci.* 48 (1), 135–152.
- Pontryagin, L.S., Boltyanskii, V.G., Gamkrelidze, R.V., Mishchenko, E.F., 1962. *The mathematical theory of optimal processes*. Interscience Publisher, John Wiley and Sons, New York.
- Ruan, W.-H., Liu, C., Guo, Z.-K., et al., 2020. The lisa–taiji network. *Nature Astron.* 4 (2), 108–109.
- Schleicher, A., Ziegler, T., Schubert, R., et al., 2018. In-orbit performance of the lisa pathfinder drag-free and attitude control system. *CEAS Space J.* 10 (4), 471–485.
- Trobbiani, L., 2014. Alternative Control Strategy for Test Mass Release of Spaceborne Inertial Sensors. University of Pisa.

- Vidano, S., Novara, C., Pagone, M., et al., 2022. The lisa dfacs: Model predictive control design for the test mass release phase. *Acta Astronaut.* 193, 731–743.
- Wang, Y., Boyd, S., 2009. Fast model predictive control using online optimization. *IEEE Trans. Control Syst. Technol.* 18 (2), 267–278.
- Wang, Z., Li, Y., 2021. State-dependent indirect pseudospectral method for nonlinear optimal control problems. *ISA Trans.* 108, 220–229.
- Yan, Z., Gong, P., Zhang, W., et al., 2020. Model predictive control of autonomous underwater vehicles for trajectory tracking with external disturbances. *Ocean Eng.* 217, 107884.
- Zanoni, C., Bortoluzzi, D., 2014. Experimental-analytical qualification of a piezoelectric mechanism for a critical space application. *IEEE/ASME Trans. Mechatron.* 20 (1), 427–437.
- Zanoni, C., Bortoluzzi, D., Conklin, J., et al., 2015. Summary of the results of the lisa-pathfinder test mass release. *Journal of Physics: Conference Series*, vol. 610, IOP Publishing, p. 012022.
- Zidek, R.A., Kolmanovsky, I.V., Bemporad, A., 2018. Spacecraft drift counteraction optimal control: Open-loop and receding horizon solutions. *J. Guidance Control Dyn.* 41 (9), 1859–1872.